AN ABSTRACT OF THE THESIS OF

Joyce Squillante for the degree of Master of Science in Radiation Health Physics presented on March 8, 2021.

Title: Dosimetry Model for Alpha Emitters in a Radioactive Skin Patch for Treatment of Early-Stage Nonmelanoma Skin Cancers.

Abstract approved:

_____

David Hamby

Nonmelanoma skin cancer (NMSC) is the most common malignancy in Caucasian populations. One existing treatment modality for NMSCs is external radiotherapy delivered to the skin cancer tumor by a beta-emitter-containing radioactive skin patch. Alpha emitters, with their higher linear energy transfer than beta particles and shorter range in tissue, make an interesting alternative treatment candidate for early-stage NMSCs. In this work, a dosimetry model is presented for the irradiation of early-stage NMSC tumors by an infinitely thin radioactive skin patch containing ^{212m}Po, a high-energy alpha emitter. The dosimetry model is compared to a Monte Carle N Particle Code (MCNP) simulation in the same geometry. Dose was assessed to three theoretical tumor thicknesses of 50, 100, and 150 μm. The dosimetry model was found to be in good agreement with the MCNP simulation. The dosimetry model calculated the cumulative doses of the three tumor thicknesses to be 86.8 Sv, 59.9 Sv, and 44.7 Sv respectively; MNCP calculated the doses to be 86.4 Sv, 64.0 Sv, and 45.6 Sv. This

corresponds to a difference between the two models of about 0.5% for the 50 μm tumor,

6% for the 100 μm tumor, and 2% for the largest of the tumor thicknesses, 150 μm.

Dosimetry Model for Alpha Emitters in a Radioactive Skin Patch for Treatment of
Early-Stage Nonmelanoma Skin Cancers

by

Joyce Squillante

A THESIS

submitted to

Oregon State University

in partial fulfillment of
the requirements for the
degree of

Master of Science

Presented March 8, 2021
Commencement June 2021

Master of Science thesis of Joyce Squillante presented on March 8, 2021

APPROVED:

_____

Major Professor, representing Radiation Health Physics

_____

Head of the School of Nuclear Science and Engineering

_____

Dean of the Graduate School

I understand that my thesis will become part of the permanent collection of Oregon State University libraries. My signature below authorizes release of my thesis to any reader upon request.

_____

Joyce Squillante, Author

TABLE OF CONTENTS

LIST OF FIGURES

LIST OF FIGURES (Continued)

LIST OF TABLES

1   Introduction

Skin cancer, including both melanoma and nonmelanoma types, is the most common malignancy in Caucasian populations (Apalla et al, 2017). Nonmelanoma skin cancer (NMSC) can be split into two main subtypes: basal-cell carcinoma (BCC) and cutaneous squamous-cell carcinoma (cSCC). While surgical excision of NMSC tumors is a common path of treatment, a variety of other options are available to patients including radiation therapy. Patients who are elderly and/or have highly visible tumors, such as on the head or neck, may prefer non-surgical treatment options for comfort and aesthetic reasons.

Radiation therapy is a valuable approach to the treatment of skin cancers. Classical forms of radiation therapy for skin cancer include electron beam therapy and X-ray therapy. More recently, skin patches or bandages, impregnated with beta emitters such as ^{166}Ho and ^{188}Re, have been designed for external application to skin cancer tumors. These skin patches are typically custom-made to the individual patient's requirements, and applied to the site of the tumor for a predetermined amount of time. This technique has been reported to be an effective NMSC treatment in rodents as well as humans (Lee et al, 1997; Pashazadeh, 2019).

Alpha particles are positively charged helium nuclei that are more than 7,000 times the mass of beta particles (Shultis and Faw, 2008). Their high linear energy transfer (LET) results in the release of large amounts of energy over very short distances. The range of alpha particles in tissue is 30-100 µm for energies of 4-10 MeV (National Institute of Standards and Technology), an energy range inclusive of most

alpha particle emissions. This is compared to the typical range for beta particles in tissue of 5,000-10,000 µm (Kim and Brechbiel, 2012; Pashazadeh, 2019). These qualities of alpha emitters provide an opportunity to target highly specific cancerous cells using an externally placed skin patch while minimizing damage to surrounding healthy tissue to an even greater effect than beta particles.

In the case of early-stage NMSCs, the cancerous cells are generally located in the epidermal layers of the skin only and have not spread into the dermis. The thickness of the epidermis is generally taken to be 100 µm or less, a range that alpha particles with relatively high energies have the ability to traverse. High-energy alpha particles are therefore an intriguing candidate for treatment of early-stage NMSC tumors located close to the surface of the skin.

The objective of this work is to provide a conceptual dosimetry model for an alpha emitter-containing skin patch for treatment of early-stage NMSC tumors. The dosimetry model provides analytical dose calculations from an infinitely thin disk-shaped skin patch, uniformly impregnated with high-energy alpha emitter ^{212m}Po, to a disk-shaped dose area below the skin surface. This model calculates total dose to three theoretical tumor thicknesses: 50 µm, 100 µm, and 150 µm. The results of the dosimetry model are compared to the probabilistic results of a geometrically similar simulation using Monte Carlo N Particle Code (MCNP).

2   Literature Review

2.1. Nonmelanoma skin cancer (NMSC)

Nonmelanoma skin cancer (NMSC) is a broad category including all malignant skin diseases that are not melanoma. The most common types of NMSCs are basal-cell carcinoma (BCC) and cutaneous squamous-cell carcinoma (cSCC), which account for the vast majority of malignancies in the NMSC category (Apalla et al, 2017). These skin cancers typically develop on areas of skin that have had frequent sun exposure, particularly on the head, neck, and shoulders. Tumors can also appear on the hands, arms, and, rarely, on parts of the body not commonly exposed to sunlight, such as the buttocks or underside of the foot (Ascierto and Schadendorf, 2019).

Basal cell carcinomas originate in the basal layers of the epidermis, the outermost layer of the skin. A slow-growing carcinoma typically appearing *de novo*, BCCs are unlikely to metastasize. On the skin, BCCs often appear smooth, similar to sores, pimples, or round growths, and tumor areas are typically red or pink in color. Darker colored tumors are more common in non-white populations (Samarasinghe and Madan, 2012). Examples of BCCs on humans can be found in Figures 1 and 2.

Figure 1: Patient with BCC on the nose. This BCC appears as a large, non-healing pimple (American Academy of Dermatology, 2020).

Figure 2: Patient with nodular BCC on the cheek. This BCC appears as a small multicolored nodule (Samarasinghe and Madan, 2012).

Cutaneous squamous cell carcinoma (cSCC) is the second most common NMSC after BCC. These most frequently arise from precancerous lesions of mutated keratinocytes, the primary cell type found in the epidermis. They are much more likely to metastasize than BCCs. Additionally, cSCCs are more varied in appearance than BCCs, often appearing as growths, open sores, age spots, or dry, scaly patches of skin. Images of cSCCs on humans can be found in Figures 3 and 4.

Figure 4: Patient with cSCC presenting as a scaly, red patch of skin. This is a common early sign of cSCC (American Academy of Dermatology, 2020).

Figure 3: Patient with cSCC on bottom of foot, presenting as a growth with raised edges. This is a cSCC that developed from a precancerous lesion (American Academy of Dermatology, 2020).

The incidence of NMSC is difficult to ascertain, as it is understudied and underreported compared to the more frequently malignant melanoma. Nonmelanoma skin cancers are associated with low mortality, but high morbidity and consequent economic burden. Although NMSCs are typically excluded from national cancer registries around the world, it is estimated that the incidence of NMSC is roughly 20 times that of melanoma, and these figures have been rising steadily for decades. It is notable that the incidence of NMSCs is considerably lower in Hispanic, Black, and other non-white populations (Apalla et al, 2017).

For many NMSC tumors, Mohs micrographic surgery or standard surgical excision are the optimum treatment methods. For patients who are unable or unwilling to undergo surgery, radiation therapy is a good alternative treatment modality. Radiation therapy can also be used in conjunction with surgery post-operatively to kill marginal tumor cells that may not have been fully excised (Samarasinghe and Madan, 2012). Other less common treatment methods for NMSC tumors include chemotherapy and immunotherapy. Radiation therapy is typically reserved for patients over 60, which is the age range most frequently affected by NMSCs, and is contraindicated in patients with genetic predisposition to skin cancer due to the high possibility of secondary cancers (Ascierto and Schadendorf, 2019; Yousef et al, 2020).

Determining the *stage* of a cancer, or its anatomic extent at diagnosis, is essential to deciding a treatment pathway for the patient. Defining stage is different between types of cancer and even anatomic site. The International Union for Cancer Control (IUCC) and American Joint Committee on Cancer (AJCC) cooperatively maintain the tumor node metastasis (TNM) system, which categorizes cancers based on the size of the primary tumor, lymph node involvement, and presence of metastasis. Though rarely required for BCCs due to their low possibility of metastasis, staging is imperative in the treatment of cSCCs due to their higher potential to metastasize. Therefore, most NMSCs including BCCs are categorized according to the cSCC TNM criteria. The staging system used for cSCCs and BCCs, from the American Joint Committee on Cancer (AJCC) can be found in Tables 1 and 2 below.

Table 1: NMSC tumor staging and high-risk tumor features (American Joint Committee on Cancer, 2010).

Primary Tumor (T)*

TX	Primary tumor cannot be assessed
T0	No evidence of primary tumor
Tis	Carcinoma in situ
T1	Tumor 2 cm or less in greatest dimension with less than two high-risk features**
T2	Tumor greater than 2 cm in greatest dimension *or* Tumor any size with two or more high-risk features**
T3	Tumor with invasion of maxilla, mandible, orbit, or temporal bone
T4	Tumor with invasion of skeleton (axial or appendicular) or perineural invasion of skull base

*Excludes cSCC of the eyelid (see Chap. 48).

**High-risk features for the primary tumor (T) staging

Depth/invasion	>2 mm thickness
	Clark level $\geq$IV
	Perineural invasion
Anatomic location	Primary site ear
	Primary site hair-bearing lip
Differentiation	Poorly differentiated or undifferentiated

Table 2: NMSC staging criteria (American Joint Committee on Cancer, 2010).

ANATOMIC STAGE/PROGNOSTIC GROUPS

Patients with primary cSCC or other cutaneous carcinomas with no evidence (clinical, radiologic, or pathologic) of regional or distant metastases are divided into two stages: Stage I for tumors measuring $\leq$2 cm in size and Stage II for those that are greater than 2 cm in size. In instances where there is clinical concern for extension of tumor into bone and radiologic evaluation has been performed (and is negative), these data may be included to support the Stage I vs. II designation. Tumors that are $\leq$2 cm in size can be upstaged to Stage II if they contain two or more high-risk features. Stage III patients are those with (1) clinical, histologic, or radiologic evidence of one solitary node measuring $\leq$3 cm in size or (2) Tumor extension into bone: maxilla, mandible, orbit, or temporal bone. Stage IV patients are those with (1) tumor with direct or perineural invasion of skull base or axial skeleton, (2) $\geq$2 lymph nodes or (3) single or multiple lymph nodes measuring >3 cm in size or (4) distant metastasis.

Stage	T	N	M
Stage 0	Tis	N0	M0
Stage I	T1	N0	M0
Stage II	T2	N0	M0
Stage III	T3	N0	M0
	T1	N1	M0
	T2	N1	M0
	T3	N1	M0
Stage IV	T1	N2	M0
	T2	N2	M0
	T3	N2	M0
	T Any	N3	M0
	T4	N Any	M0
	T Any	N Any	M1

Of particular interest in this research are the earlier stages of NMSCs, namely Stage 0 and Stage I. The most commonly diagnosed new cases of NMSCs fall into these stages. Features of early-stage NMSC tumors include a diameter of $\leq$2 cm and no metastasis. In the case of Stage 0, the tumor is contained solely to the epidermis. These cancers have not typically spread into the dermis, making them attractive candidates for short-range radiation therapy like an alpha emitter containing skin patch (American Joint Committee on Cancer, 2010). Stage II NMSCs have the potential to be treated in this manner as well, if the cancer has not invaded the dermis, or has only minimally invaded the dermis in places where the epidermis is thinner. More complicated NMSC

cases, such as those with local or distant metastasis, are not ideal candidates for this type of treatment.

2.1.1. Layers of skin

Skin is composed of three layers: the epidermis, dermis, and hypodermis. The epidermis is the outermost layer of skin and can vary widely in thickness due to its many sub-layers. The dermis lies deep to the epidermis, connected to it by the basal lamina. The hypodermis is further deep to the dermis and is primarily composed of adipose fat tissue. Figure 5 shows a cross-section of skin with each of these layers labeled. Early-stage NMSCs are typically confined to the epidermis, infiltrating the dermis in more aggressive cases. Therefore, the epidermis will be the focus of this discussion (Yousef et al, 2020).
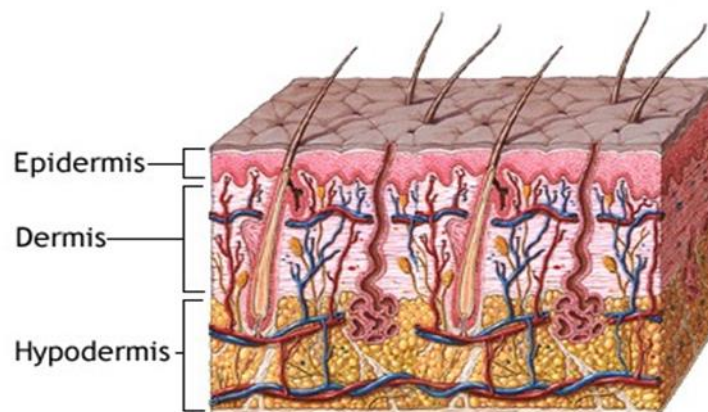
Figure 5: Cross section of skin with the main layers labeled (Heller et al, 2019).

The epidermis consists of several layers, as shown in Figure 6. The outermost layer is the *stratum corneum*, which is approximately 10-30 cell layers and consists of dead keratinocytes. It is the layer that varies the most in thickness. The cells in this

layer continuously shed, with complete cell turnover taking about four weeks for adults. The *stratum lucidum*, making up 2-3 cell layers of dead keratinocytes, is only present on the palms of the hands and soles of the feet, providing an extra layer of skin thickness to these specific areas. The *stratum granulosum* contains keratinocytes that are beginning to flatten and die, and the cells are "glued" together in their migration to the skin surface. As the cells die, they leave behind the keratin and thick membranes that form the *stratum lucidum.* The *stratum spinosum*, or the squamous cell layer, is 8-10 cell layers and consists of maturing keratinocytes, or squamous cells, that have come from the *stratum basale*.
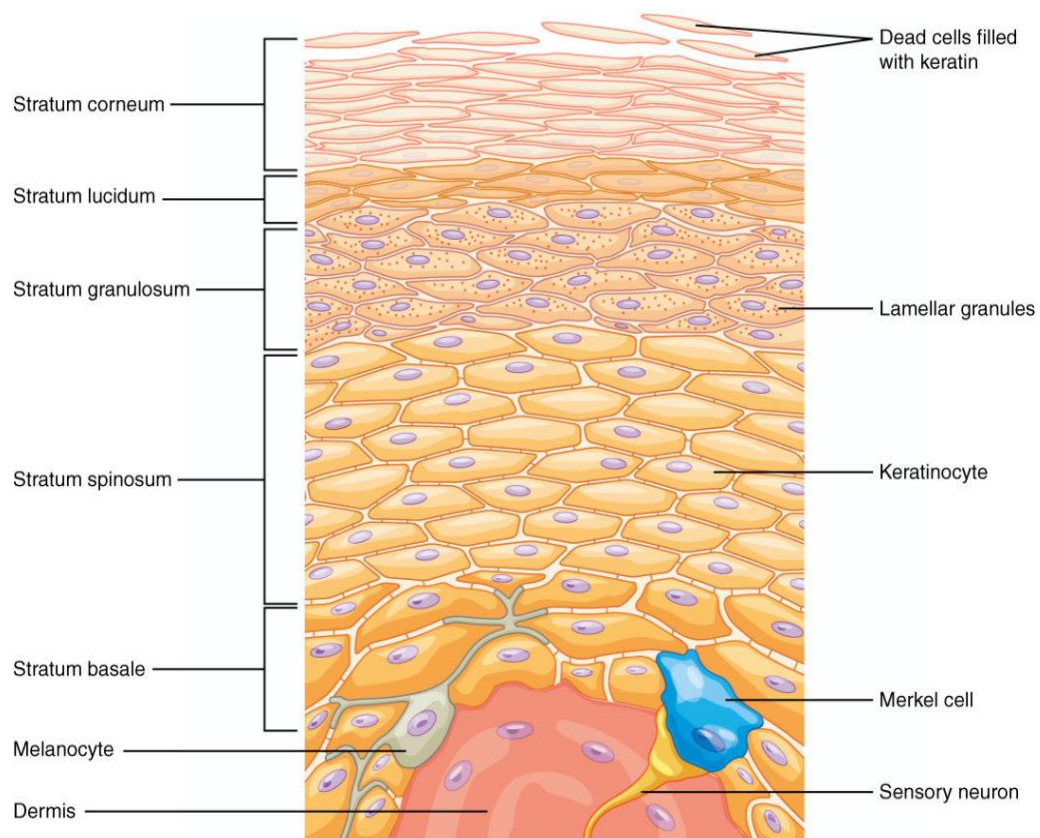
Figure 6: Layers of the epidermis (Betts et al, 2013).

Also referred to as the basal layer, the *stratum basale* is the innermost layer of the epidermis and contains a single layer of active stem cells that continuously produce keratinocytes. The keratinocytes then migrate superficially to the squamous cell layer. The basal layer also contains Merkel cells which, like the other cells of the basal layer, have the ability to proliferate uncontrollably and lead to what is referred to as Merkel-cell carcinoma (MCC). MCC is a subtype of NMSC that is extremely rare and typically aggressive and difficult to treat (and is therefore left out of the scope of this discussion). Lastly, melanocytes produce the pigment melanin; cancer of the melanocytes is referred to as melanoma, which is excluded from NMSC discussions (Betts et al, 2013; Yousef et al, 2020).

The dermis, lying deep to the epidermis, consists of two layers of connective tissue. The papillary layer is the uppermost layer and is in contact with the epidermis. The reticular layer, deep to the papillary layer, is filled with dense connective tissue and collagen fibers. The dermis hosts a variety of structures including hair follicles, blood vessels, nerves, and sebaceous glands (Yousef et al, 2020).

2.1.2. Epidermal thickness

The thickness of the epidermis varies widely with body site and may also be impacted by other factors including age, sex, skin pigmentation, and tobacco use. Epidermal thickness also varies greatly on an individual basis (Sandby-Møller et al, 2003). Therefore, what appear to be two similarly-sized NMSC tumors on different body sites could require vastly different treatment modalities. Awareness of epidermal

thickness and accurate epidermal measurements are particularly important in alpha particle skin dosimetry, due to alpha particles' already-limited range in tissue.

Several studies have been performed to find the average thickness of the epidermis at different body sites. Whitton (1973) measured epidermal thickness at six main body sites from 188 volunteers: head, trunk, arms and legs, backs of hands, wrists, and fingers. Sevcova et al (1978) sought to verify Whitton's data by measuring epidermal thickness at additional body sites that were less likely to be covered by clothing, such as the cheeks, forehead, and neck. These data are summarized in Table 3.

Table 3: Comparison of epidermal thickness results from Sevcova et al (1978) and Whitton (1973). Table adapted from Sevcova et al (1978).

Body site	Sevcova et al (1978)			Whitton (1973)		
	# of samples, N	Average epidermal thickness (mg/cm^2)	σ (mg/cm^2)	# of samples, N	Average epidermal thickness (mg/cm^2)	σ (mg/cm^2)
Forehead	18	5.7	1.96	17	5.5	2.22
Cheek	14	6.4	1.96	3	4.3	1.07
Neck	3	4.4	0.30	-	-	-
Trunk	6	4.2	2.10	7	4.1	1.22
Arm	17	4.9	1.42	7	5.8	2.85
Back	14	5.5	1.25	24	4.8	1.47

Table 3 confirms that the thickness of the epidermis varies widely by body site. Additionally, many of the averages in each study have high standards of deviation, indicating a large epidermal thickness variation by individual. This individual variation has been validated other times in the literature (Sandby-Møller et al, 2003). While many aspects of what factors influence epidermal thickness are being studied, it is clear from the existing evidence that body site and individual variability play essential roles.

The results from Whitton and Sevcova et al are in good agreement with each other. In general, it can be seen that the thickness of the epidermis typically fits within the 45-

65 μm range (assuming $\rho = 1$ g/cm^3) across most body sites. This range is very traversable by high energy alpha particles such as those from ^{212m}Po.

2.2. Radioactive skin patches as treatments for NMSCs

Several forms of radiation therapy for skin cancers exist in medicine, including the use of electron beams, neutron beams, and X-rays. A relatively recent form of brachytherapy, in the form of an externally placed skin patch uniformly impregnated with a beta-emitting radionuclide, has been reported with success in both murine and human models (Lee et al, 1997; Pashazadeh, 2019).

In the application of such a skin patch, the tumor is first measured, and a layer of cream or other gel is placed on the tumor to protect the skin from direct radioactive contamination. The radionuclide, in a chemically stable form, is impregnated in a scaffold, paper, or mixed with a resin material to form a mold that can be shaped to the patient's tumor. The patch is then placed on the tumor for an amount of time to deliver a predetermined dose. Radionuclides that have been reported to be effective in treating superficial skin cancer tumors in this manner include ^{166}Ho, ^{188}Re, ^{90}Y, and ^{32}P (Munaweera et al, 2014; Pashazadeh, 2019). Beta emitters, with a range in skin of about 5-10 mm, make an interesting choice for external radiation therapy.

There are several benefits of the radioactive skin patch treatment method over other types of NMSC treatment. The skin patch is less costly when compared to more traditional radiation therapy techniques, due to the latter's association with large, expensive equipment like linear accelerators. Additionally, since the patch is specially designed to the patient's tumor, the ability of the radiation to kill more cancerous cells

while leaving the healthy surrounding tissue undamaged is greater. In cases where surgery is contraindicated, or for patients who do not wish to undergo surgery, this form of radiation therapy is a feasible alternative method of treatment.

Radioactive skin patches can also be used in conjunction with surgery as a post-operative method of irradiating any cancer cells that may have been left over after surgical removal. This is not unlike the use of ^{131}I to ablate thyroid cancer in conjunction with partial or total thyroidectomy, to ensure more complete cancer cell kill (Pashazadeh, 2019).

2.3. Targeted alpha particle therapy (TAT)

The use of alpha emitters in radiation therapy is not novel. With their short path length and densely ionizing particle track, alpha emitters have been considered for their potential cancer-treating properties for decades. Alpha particles have the unique ability to kill individual tumor cells with only self-irradiation, which is generally not achievable with beta particles. Evidence suggests that it may be more efficient to target a small number of cancer tumor stem cells, as opposed to targeting all tumor cells, to increase treatment effectiveness. The ability of alpha particles to target highly specific cells while exhibiting a relatively low toxicity profile may be able to satisfy this need (Sgouros et al, 2010).

Targeted alpha particle therapy (TAT) has been used in clinical research since the mid-1990s. To date, the only alpha emitter that has been approved for medical use in the United States is ^{223}Ra, for treatment of metastatic bone cancers. In research trials, alpha emitters have shown promising results in treatments of leukemias, lymphomas,

and gliomas. Most relevantly to the scope of this research, a clinical study by Allen et al (2005) used intralesional administration of ^{213}Bi, an alpha emitter, in a trial with 16 melanoma patients. The study found that ^{213}Bi led to significant melanoma cell killing and resolution of tumors: "…the results showed that intralesional TAT is non-toxic and locally efficacious up to 1350 µCi … and the histology showed almost complete cell kill at 450 µCi and above with few viable cell clusters" (Allen et al, 2005).

While beta emitters are more widely available and predominately used in targeted radionuclide therapy research studies, TAT continues to be an area of interest for researchers due to the unique properties of alpha particles. Currently, TAT research is primarily limited by the availability and cost-effectiveness of alpha emitters. Improved knowledge of the radiochemistry of alpha emitters and their stability is also imperative to TAT development (Lassman and Eiberlein, 2017).

3 Theory

3.1. Alpha decay and energetics

Alpha particles are identical to helium nuclei, consisting of two protons and two neutrons, carrying a net charge of +2. The alpha particle is more than 7000 times the mass of an electron. The most common source of alpha particles is alpha decay of heavy, unstable nuclei (Shultis and Faw, 2008). A schematic of alpha decay is shown in Figure 7.

Heavy atomic nuclei with low neutron-to-proton ratios are more likely to undergo alpha decay to achieve stability. Alpha decay is possible for all nuclides with
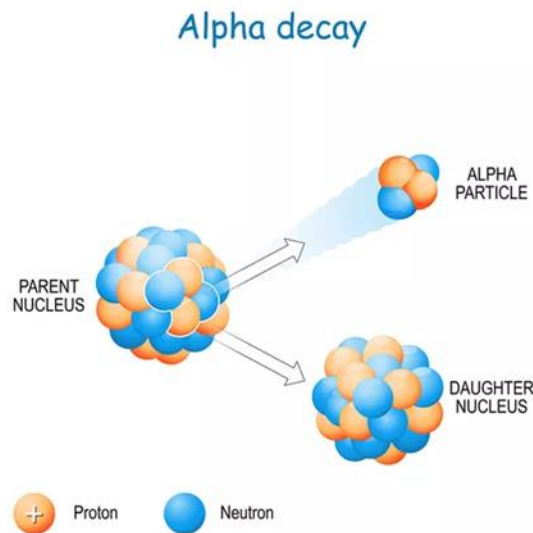
Figure 7: Schematic of alpha particle decay (Getty Images).

atomic number $Z \geq 83$. While alpha decay has been observed in some unusually light nuclei, such as ^{8}Be which decays via two alpha emissions, it is the predominant decay process only for nuclei with mass numbers $A \geq 210$ (Shultis and Faw, 2008). This can be seen in Figure 8, which shows the Chart of Nuclides with different types of radioactive decay color-coded. The yellow boxes represent nuclides that predominately undergo alpha decay, which is seen to mainly occur in proton-rich nuclei over $Z = 82$.

In alpha decay, an atomic nucleus emits two protons and two neutrons (an alpha particle) resulting in a mass reduction of four and a nuclear charge reduction of two. The nucleus will sometimes be left in an excited state, requiring the emission of a gamma ray to bring the nucleus to ground state. The emission of an alpha particle lowers the Coulombic energy of the nucleus by decreasing its size, in turn increasing its stability (Knoll, 2000).
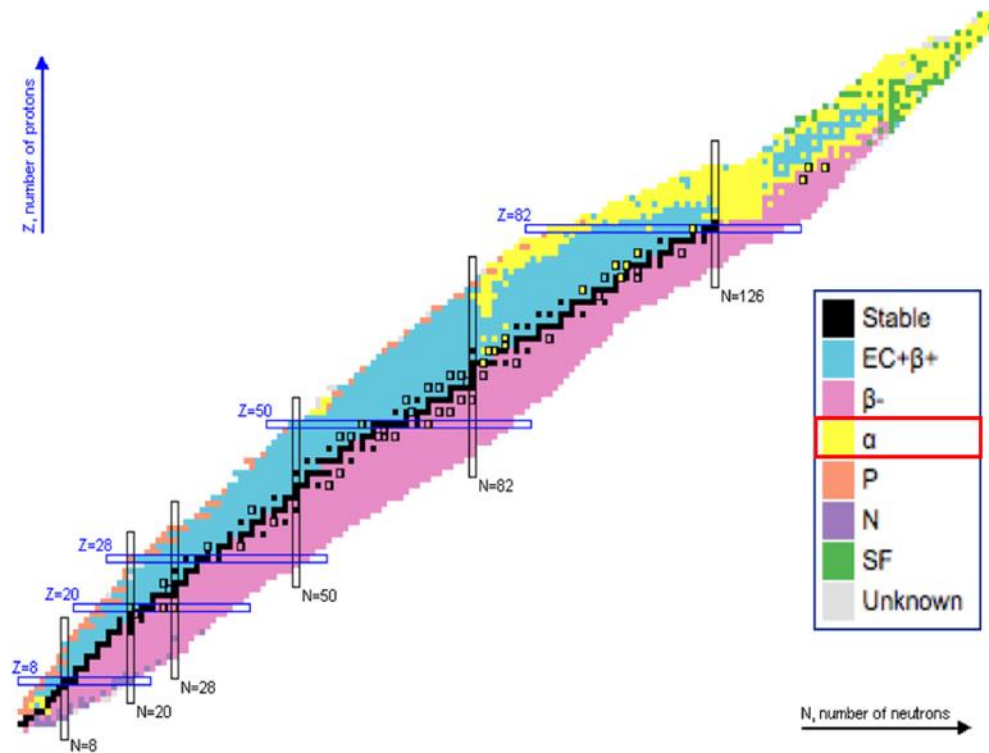
Figure 8: Chart of Nuclides with decay modes shown (legend emphasis author's). The yellow boxes represent nuclides that decay primarily via alpha emission (Woolsey, 2018).

While average alpha particle energies are in the 3-8 MeV range, there are radionuclides with especially heavy nuclei that can emit alpha particles with energies upwards of 15 MeV.

3.1.1. Alpha particle interactions in matter

As alpha particles traverse through matter, they are continuously interacting with the surrounding material. Alpha particles, with their doubly positive charge, frequently interact with the outer electrons of the atoms in the material through which they traverse. With each interaction, energy is transferred from the alpha particle to loosely bound electrons and the velocity of the alpha particle slows. Because of alpha particles' high energies, these particles must undergo many interactions to completely

lose their energy. Alpha particles primarily lose energy by the mechanisms of ionization and excitation (Knoll, 2000).

In an ionization event, an alpha particle provides a sufficient attractive Coulombic force to a nearby atom that results in the removal of one or more of its electrons, *ionizing* the atom. This is more likely to occur with atoms that are closer to the particle's track (Knoll, 2000).

In an excitation event, the attractive force exerted by the alpha particle is insufficient to remove an electron from a nearby atom. In these cases, the electron is instead raised to a higher energy state, *exciting* the atom. This is more likely to occur with atoms that are farther from the alpha particle's trajectory. When excited, the atom will emit a low-energy photon in its de-excitation to ground state. At lower energies, alpha particles are more likely to lose energy through excitation than ionization (Knoll, 2000).

3.1.2. Stopping power and Bragg curve

A crucial parameter in charged particle dosimetry is the differential energy lost by the particle per unit path length. This is referred to as the particle's *stopping power* and is described in its linear form in Equation 1.

$$S = -\frac{dE}{dx} \qquad (1)$$

A more useful expression of this quantity is *mass stopping power*, which lets the stopping power become mostly independent of the material's density. This is achieved by dividing the stopping power by the density of the material, shown in Equation 2. Mass stopping power is conventionally expressed in units of (MeV$\cdot$ cm^2/g).

$$\frac{S}{\rho} = -\frac{dE/dx}{\rho} \qquad (2)$$

Stopping power for heavy charged particles such as alpha particles increases drastically towards the end of the particle's path. As the particle traverses farther into the medium, its velocity is continually slowing. As it slows, the rate of energy transferred to the medium increases. This is demonstrated in the Bragg curve, a graph that shows the stopping power versus the distance into the material the particle has traversed (Knoll, 2000). Sample Bragg curves for two alpha particles in water are provided in Figure 9.

It is seen in Figure 9 that much of the energy from each alpha particle is deposited towards the end of the particle's track, at what is known as the Bragg peak.
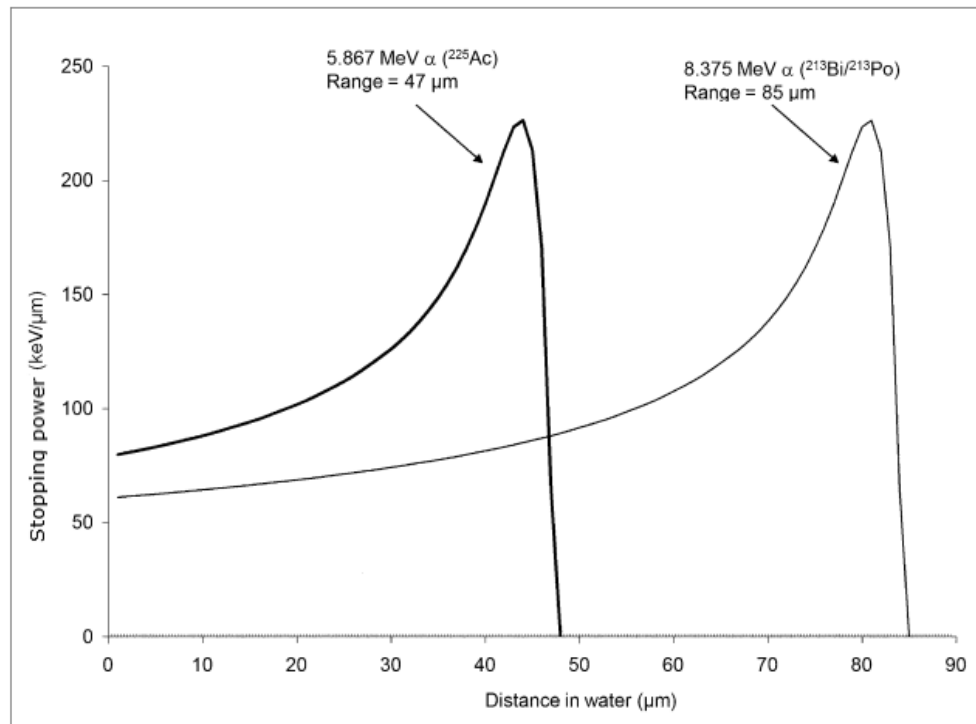
Figure 9: Stopping power vs distance in water for two alpha energies (Bragg curves) (adapted from Sgouros et al, 2010).

3.1.3. Energy straggling

Although alpha particles are considered essentially monoenergetic, their energy loss is actually subject to variation. This is due to the random nature of charged particle interactions with matter. Because a large number of interactions are required to completely slow an alpha particle, statistical variation occurs in both the total number of collisions and the amount of energy lost in each collision. Therefore, a group of initially monoenergetic alpha particles will have a distribution of energies as they traverse a given thickness. This effect is referred to as *energy straggling.* Energy straggling is more noticeable at lower energies, as charged particles begin to deflect more broadly from the atomic nuclei they pass (Knoll, 2000; Turner, 2007).

3.1.4. Alpha particle range in materials

Unlike beta particles, which have small mass and crooked, meandering ranges, alpha particles have short, mostly straight path lengths. Alpha particles have short range in most materials, with higher-energy particles being able to penetrate farther into tissue. In tissue, the range of most alpha particles is between 50-100 µm. The range is limited primarily by the large mass of the alpha particle (Turner, 2007).

There are several definitions of heavy charged particle range. The *mean range* is the range at which the overall fraction of particles reaching a particular distance is halved. The more standard way of defining range is called the *continuous slowing-down approximation (CSDA) range*, which is obtained by viewing the overall energy loss of the alpha particle as a continuous process. For the scope of this work, these definitions of range are essentially the same (Shultis and Faw, 2008).

3.1.4.1. Range straggling

Much like the phenomenon of energy straggling, heavy charged particles including alpha particles are also subject to *range straggling.* The exact amount of energy lost per particle interaction varies, and these same statistic variations lead to a range straggling effect. The straggling effect can be seen in Figure 10 as the derivative of the solid line curve. The solid line curve represents the fraction of particles that reach a particular distance *s*. The mean range ($\bar{R}$) and the extrapolated range (R_e), obtained by extending the tangent of the curve at its point of inflection to zero, can be seen in Figure 10 as well (Shultis and Faw, 2008).
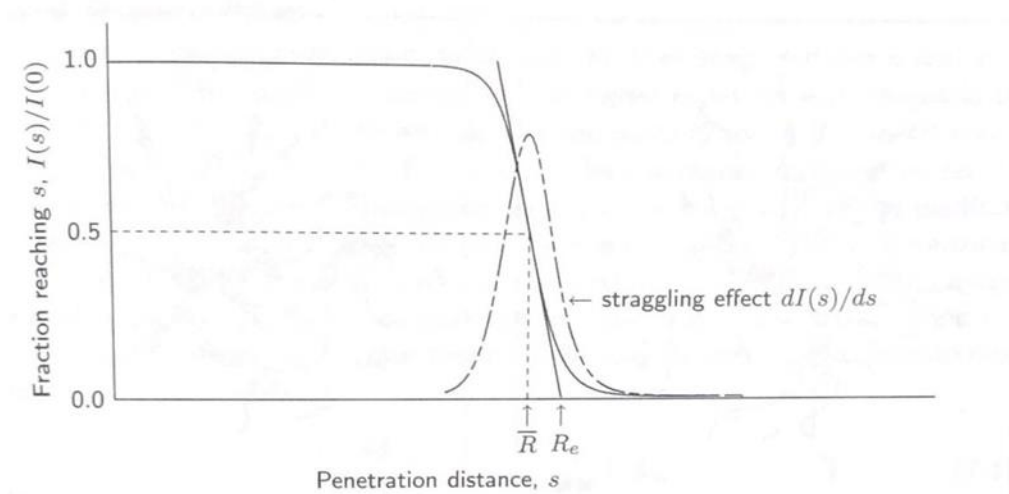
Figure 10: Range straggling effect. Fraction of alpha particles that penetrate a distance s. The dotted curve is termed the "straggling curve." Mean range and extrapolated range are labeled (adapted from Shultis and Faw, 2008).

Figure 10 demonstrates that the range of alpha particles is subject to some amount of variation. This phenomenon is particularly important in radiation dosimetry, as alpha particle ranges in tissue are on the magnitude of microns. Seemingly minor

fluctuations towards the end of an alpha particle's range can spell much larger issues for radiation therapy treatment because energy deposition is greatest at the end of its tracks (Turner, 2007).

3.1.4.2.   Bragg-Kleeman rule

The range of alpha particles at a given energy, if known for one material, can be estimated for other materials using the Bragg-Kleeman rule. Traditionally, the Bragg-Kleeman rule compares the range of alpha particles in air to some other material. The range of alpha particles of a particular energy in tissue is not precisely known, but it can be estimated by the following version of the Bragg-Kleeman rule (Eq. 3),

$$R_{tissue} = \sqrt{\frac{M_{tissue}}{M_{air}}} * \frac{R_{air}\rho_{air}}{\rho_{tissue}} \qquad (3)$$

where M is the atomic weight (in g/mol) of the material, and ρ is the density of the material (in g/cm^3) (Knoll, 2000).

3.2. Dosimetry concepts and terminology

3.2.1. Linear energy transfer (LET)

A concept closely related to stopping power is that of linear energy transfer (LET). While stopping power is a measure of differential energy loss per unit path length, LET describes local energy transfer in the material through which the particle is traveling. LET is considered a volume-limited form of stopping power. This is relevant in radiotherapy, where radiation treatments are typically administered to a definitive tumor size (Sgouros et al, 2010).

High-LET radiations, such as those from heavy charged particles like alpha particles, lead to greater biological damage than low-LET radiations like that of beta particles. This means alpha particles have more effective cell killing ability than beta particles or other low-LET radiations (Knoll, 2000), which is one of the features of alpha decay that makes it such an intriguing candidate for radiotherapy.

3.2.2. Absorbed dose

The mean energy imparted by ionizing radiation to a specific volume of matter, divided by the mass of that volume, is defined as *absorbed dose* (Eq. 4). Absorbed dose is conventionally expressed in units of Gray (Gy = J/kg).

$$D = \frac{d\bar{\varepsilon}}{dm} = \frac{mean\ energy\ imparted}{mass} \qquad (4)$$

Absorbed dose in tissue is a fundamental quantity in radiobiology, radiation therapy, and dosimetry as it is the measurement of the amount of energy the radiation is imparting to the target tissue (Knoll, 2000).

3.2.3. Radiation weighting factors

As discussed previously, alpha particles are considered high LET radiation, meaning that they deposit very large amounts of energy over relatively short distances. The LET of an alpha particle is much greater than that of low-LET radiations like that of beta particles.

Relative biological effectiveness (RBE) is a measure of the biological effectiveness of one type of radiation compared to another. High-LET radiations are

more effective at cell killing than low-LET radiations, therefore making them more biologically hazardous. This means that high-LET radiations have higher RBE than low-LET radiations (Knoll, 2000).

To account for RBE between radiations, the International Commission on Radiological Protection (ICRP) has defined a set of radiation weighting factors for use in dosimetry calculations. The current ICRP recommendations for radiation weighting factors, summed up in Table 4, have been in use since the adoption of ICRP Publication 60 (1977). It can be seen from Table 4 that the radiation weighting factor for alpha particles is 20 (ICRP Publication 103, 2007).

Table 4: Recommended radiation weighting factors (ICRP, 2007).

Radiation type	Radiation weighting factor, w_R
Photons	1
Electrons[a] and muons	1
Protons and charged pions	2
Alpha particles, fission fragments, heavy ions	20
Neutrons	A continuous function of neutron energy (see Fig. 1 and Eq. 4.3)

All values relate to the radiation incident on the body or, for internal radiation sources, emitted from the incorporated radionuclide(s).
  [a] Note the special issue of Auger electrons discussed in paragraph 116 and in Section B.3.3 of Annex B.

3.2.4. Dose equivalent

Dose equivalent is defined as the product of absorbed dose in tissue and the relevant radiation weighting factor (Eq. 5). The associated unit for dose equivalent is

the Sievert (Sv), identical to the Gray but conventionally used in place of Gray when calculating dose equivalent.

$$H = D * w_R \quad (5)$$

In equation 5, H is the dose equivalent, D is the absorbed dose, and w_R is the radiation weighting factor, which can be taken from Table 4 (Knoll, 2000; Turner, 2007).

3.3. Point kernel concept for total dose equivalent

Calculating dose to a target area is made considerably easier by the use of the point kernel method. This concept divides a volume source and/or target into elementary "point kernels," source points and dose points. Each source point contributes to dose based on the distance between the individual source and dose points in question (Prokhorets et al, 2007). The point kernel method can be used if the following conditions are met: the source emits radiation isotropically with a consistent energy spectrum at all source points; the detector can equally detect radiation from any direction; and the source and target are located in an infinite homogenous medium (Shultis and Faw, 1996). These three conditions are modeled in this work.

Shultis and Faw (1996) gave the following (Eq. 6) as a sample or general point kernel for heavy charged particles,

$$G(r, E_0) = \frac{L(\Lambda(E_0) - r)}{4\pi r^2 \rho} \qquad if \ r < \Lambda(E_0) \qquad (6)$$

where $L(\varLambda)$ is the collisional stopping power of a heavy charged particle with range $\varLambda$. The point kernel $G(r, E_0)$ is the energy deposited per unit mass of the medium which is a distance r from the source. The initial source energy is represented by E_0 and the material density is represented by ρ.

3.4. Integrated activity

When the activity of the radionuclide in question is changing considerably relative to the patch deployment time, special consideration needs to be taken in the form of "integrated activity." In this work, the assumed source nuclide, ^{212m}Po, has a very short radioactive half-life of 45 seconds, and the patch is placed on skin for time periods on the order of minutes. This time accounts for the decay of a large fraction of the radioactive atoms, and integrated activity (total energy deposition) must be considered.

To consider this factor, the radioactivity of the source is integrated with respect to exposure time to get the total number of disintegrations in that time:

$$U_s = A_0 \int_0^\tau e^{-\lambda t} dt$$

where U_s is the integrated activity, A_0 is the initial activity, λ is the radioactive decay constant, and τ is the exposure time. This can be integrated to find (Eq. 7):

$$U_s = \frac{A_0}{\lambda}(1 - \exp(-\lambda \tau)) \quad (7)$$

4   Method

This work presents an analytical dose-averaged alpha particle dosimetry model for an infinitely thin radioactive skin patch uniformly impregnated with ^{212m}Po, a high-energy alpha-emitting nuclide. Dose equivalent was calculated to three theoretical tumor thicknesses: 50 µm, 100 µm, and 150 µm. Results were compared to Monte Carlo N Particle simulations in similar geometry.

4.1. Decay routes of ^{212m}Po

The metastable state of ^{212}Po emits three high-energy alpha particles. Most notably, an 11.66 MeV alpha particle is emitted from ^{212m}Po with 96.9% yield. With this high energy alpha emission and a half-life of 45 seconds, ^{212m}Po makes a fascinating candidate for an alpha-emitter-containing radioactive skin patch. This isotope of polonium decays via alpha emission to stable ^{208}Po, so decaying daughter nuclides are not a dosimetric concern. The decay scheme for ^{212m}Po is found in Figure 11.
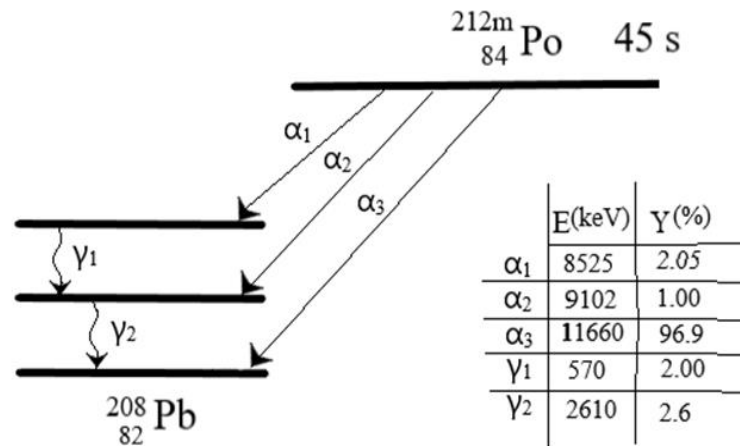
Figure 11: Decay scheme for ^{212m}Po.

The decay products of ^{212m}Po also include alpha particles of 9.1 MeV (Y = 1%) and 8.53 MeV (Y = 2.1%). These alpha particles are associated with low-probability gamma ray emissions to ground state, with energies corresponding to 2610 keV (Y = 2.6%) and 570 keV (Y = 2%), respectively. The known emissions of ^{212m}Po are summarized in Table 5. For the scope of this research, decay routes other than the 11.66 MeV alpha emission (α_3 in Figure 11) are ignored.

Table 5: The decay pathways of 212mPo (adapted from IAEA – Nuclear Data Section).

Alpha emissions		Gamma emissions	
Eα [MeV]	Yield [%]	Eγ [keV]	Yield [%]
8.53	2.1	570	2.0
9.10	1.00	2610	2.6
11.66	96.9		

4.2. NCSS Statistical Software

ICRU 90 (2014) updated a series of stopping power and range tables for alpha particles in air, liquid water, and graphite up to 15 MeV. The tables for alpha particles

in air and liquid water were uploaded into a software called NCSS Statistical Software (2020). NCSS provides its users with a comprehensive library of statistical tools and graphing options for a wide variety of data analytics purposes.

NCSS was used to create three fit equations: one for mass stopping power in water as a function of particle energy; density range in air as a function of energy; and energy as a "function" of density range in air. The data used to fit these three equations were pulled directly from ICRU 90 (2014) and can be found in abridged form in Appendix A.

Among several curve fitting options, NCSS has a "Ratio of Polynomial Search – One Variable" option, which allows the user to select the dependent and independent variables to be fit, as well as variable transformation options that may be appropriate. The software analyzes all possible model options from the user's input and makes suggestions for the best model fits for the data. An example of the "Ratio of Polynomial Search – One Variable" output report, for a fit of density range in air as a function of particle energy, can be seen in Table 6 below:

Table 6: Output report for the Ratio of Polynomials Search curve fitting option in NCSS.

Ratio of Polynomials Search Report

Dataset   C:\Users\joyce\Documents\NCSS 2020\VOGUE_NCSS.NCSS
Dependent (Y)   Density_Range
Independent (X) Energy

Search Summary Section

Model No.	F(Y)	F(X)	Model	Current R-Squared	Best R-Squared	Percent of Best
1	LN(y)	SQRT(x)	5 / 5	1.000000	1.000000	100.00
2	LN(y)	SQRT(x)	4 / 5	1.000000	1.000000	100.00
3	LN(y)	SQRT(x)	4 / 4	1.000000	1.000000	100.00
4	1/SQRT(y)	SQRT(x)	5 / 5	1.000000	1.000000	100.00
5	y	LN(x)	5 / 5	1.000000	1.000000	100.00
6	SQRT(y)	SQRT(x)	5 / 5	1.000000	1.000000	100.00
7	y	SQRT(x)	4 / 4	1.000000	1.000000	100.00
8	y	SQRT(x)	4 / 5	1.000000	1.000000	100.00
9	y	SQRT(x)	5 / 5	1.000000	1.000000	100.00
10	LN(y)	LN(x)	5 / 5	1.000000	1.000000	100.00
11	SQRT(y)	SQRT(x)	3 / 5	1.000000	1.000000	100.00
12	1/SQRT(y)	SQRT(x)	4 / 5	1.000000	1.000000	100.00
13	y	SQRT(x)	3 / 5	1.000000	1.000000	100.00
14	SQRT(y)	SQRT(x)	3 / 4	1.000000	1.000000	100.00
15	SQRT(y)	SQRT(x)	3 / 3	1.000000	1.000000	100.00
16	SQRT(y)	LN(x)	4 / 4	1.000000	1.000000	100.00
17	LN(y)	SQRT(x)	1 / 5	1.000000	1.000000	100.00
18	SQRT(y)	LN(x)	5 / 5	1.000000	1.000000	100.00
19	y	SQRT(x)	3 / 4	1.000000	1.000000	100.00
20	1/SQRT(y)	SQRT(x)	1 / 5	1.000000	1.000000	100.00

The output report lists what the software found to be the 20 best models that fit the input data, accounting for any transformations of *x* or *y* the user chooses to include. The fourth column of Table 6 describes the model as the order polynomial in the numerator over the order polynomial in the denominator. NCSS also provides each model's expected R^2 value. The search report was then used to narrow down which models would be fitted for the data. For example, the first model option in Table 6 would follow the form:

$$\ln(\Lambda\rho_{air}) = \frac{\sqrt{E} + (\sqrt{E})^2 + (\sqrt{E})^3 + (\sqrt{E})^4 + (\sqrt{E})^5}{\sqrt{E} + (\sqrt{E})^2 + (\sqrt{E})^3 + (\sqrt{E})^4 + (\sqrt{E})^5}$$

After a Ratio of Polynomials search was carried out, the "Ratio of Polynomials Fit – One Variable" curve fitting option was used to establish the chosen model and its coefficients. It should be noted that while the search output suggests models in order

of "best to worst" fit, not all of the suggested model options actually produced fit equations for the data when run in the Ratio of Polynomials Fit function. Of the first 3-5 model suggestions that were tried for each data set, the best option was chosen to fit the data.

Running the selected model in the Ratio of Polynomials Fit option provided a convergence test and coefficients for the chosen model, in addition to other statistical information including variance and standard deviation for the data sets. This procedure was used to find fit equations for mass stopping power in water, density range in air, and energy. These fit equations can be found in Eq. 8-10.

$$\Lambda\rho_{air} = EXP\left(\frac{-14.96898 - 192.5433\sqrt{E} + 187.0846E - 175.3049(E)^{\frac{3}{2}} + 13.24883E^2}{1 + 23.30342\sqrt{E} - 16.47945E + 13.72544(E)^{\frac{3}{2}} + 3.416341E^2}\right) \quad (8)$$

$$E = \frac{-3.447587 - 1.248744(\ln(\Lambda\rho_{air})) - 0.1711394\left(\ln(\Lambda\rho_{air})\right)^2 - 0.01046125(\ln(\Lambda\rho_{air}))^3 - 30.06026(\ln(\Lambda\rho_{air}))^4}{1 + 1.047572(\ln(\Lambda\rho_{air})) + 0.4176743(\ln(\Lambda\rho_{air}))^2 + 0.08294695(\ln(\Lambda\rho_{air}))^3 + 0.008196484(\ln(\Lambda\rho_{air}))^4 - 0.0003223555(\ln(\Lambda\rho_{air}))^5} \quad (9)$$

$$\frac{S}{\rho} =$$

$$\frac{2187.7 - 2.57008(\ln E) + 942.6795(\ln E)^2 + 7.422102(\ln E)^3 - 30.06026(\ln E)^4 - 4.952705(\ln E)^5}{1 + 0.2338179(\ln E) + 0.8293901(\ln E)^2 + 0.1650164(\ln E)^3 + 0.1138328(\ln E)^4 - 0.005094198(\ln E)^5}$$

$$(10)$$

4.3. Analytical dosimetry method

Dose calculations centrally involved use of the point kernel method discussed in section 3.3. Although the dosimetry scenario is that of a disk source and disk-shaped target area, stopping power determinations were carried out by temporarily remodeling

the scenario as a point source geometry, with a single point source located at the center of the theoretical skin patch. The dose-disk was therefore shrunk down to an "effective" dose area that encapsulated the portion of the dose-disk traversable by a single ^{212m}Po alpha particle emitted from the modeled point source at the center of the patch. This effective dose area was then split into ten concentric annuli. Dose was calculated to each annulus and a weighted sum determined to get the dose to the effective dose area. This weighted dose was then multiplied by an "average flux" factor to extrapolate the dose from the effective dose area to the entire dose-disk.

This process was repeated at 0.1 µm tissue depths beginning at 0.1 µm below the skin surface and extending to the end of the range of the alpha particles. At each discrete tissue depth, an average flux factor was calculated in the disk source-disk target geometry. Then, the geometry was temporarily modeled as a point source geometry in order to determine particle travel length, residual range and energy, and therefore stopping power, for use in Equation 6.

Volume-averaged dose to three theoretical tumor thicknesses (0-50 µm, 0-100 µm, and 0-150 µm) was calculated by averaging discrete doses at 0.1 µm depths over the depth range of the tumor of interest. Microsoft Excel in conjunction with Visual Basic for Applications (VBA) was used for all calculations in this section.

4.3.1. Scenario geometry

The radioactive skin patch was modeled to be an infinitely thin planar disk source with a radius of 1 cm. This size matches the typical maximum dimension of an early-stage NMSC tumor, whereas tumor sizes greater than 1 cm in radius indicate

more complicated or invasive cancers (American Joint Committee on Cancer, 2010). This is also consistent with the sizes of the beta-emitting skin patches that have been discussed in the literature (Pashazadeh, 2019).

An infinitely thin disk-shaped dose averaging area, or dose-disk, below the surface of the skin was assumed to have an area of 3.14 cm^2, matching the source radius and area. The tissue depth between the source disk and the dose-disk was varied between 0.1 µm under the skin surface and the maximum range of the alpha particles. Dose was calculated to discrete dose areas at each 0.1 µm depth, to later be averaged over each tumor depth region to result in volume-averaged tumor dose. Figure 12 shows a diagram of this geometry, where R_s is the radius of the source, and R_d is the radius of the dose-disk. The variable Λ represents the range of the alpha particle if emitted from the center of the source to the farthest point it could theoretically reach on the dose-disk. R_{eff} will be discussed in a later section.
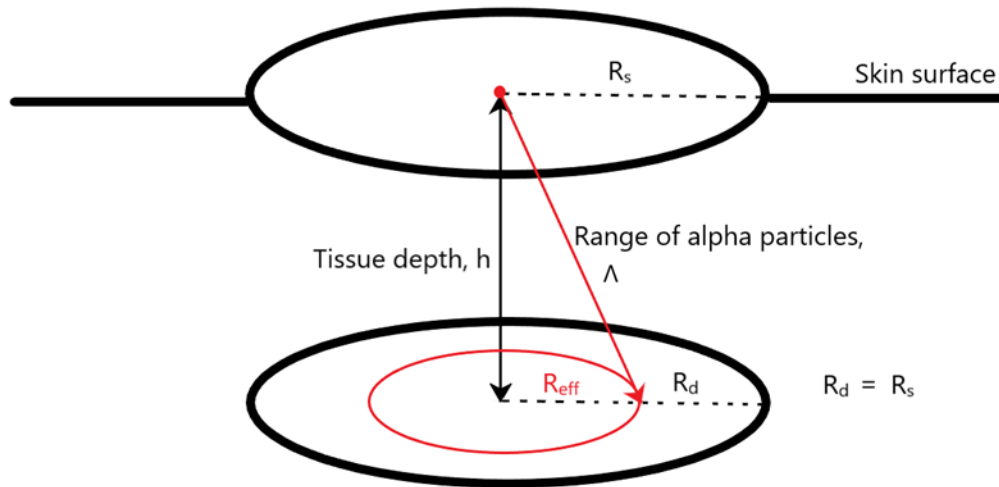
Figure 12: Diagram of scenario geometry.

4.3.2. "Average flux" factor

Flux is loosely defined as the rate at which particles or photons from a radioactive source pass through a dosimetric target. Flux is often determined solely by the uncollided radiation from source to target; in the analytical method section of this work, any scattering or interactions from surrounding materials or secondary radiation is ignored. To conceptualize flux for this scenario's geometry, picture a particle emitted from an infinitesimally small portion of the source disk reaching a point P in the dose area off-axis from the origin of the disk source (for example, along the red arrow in Figure 12). This geometry is outlined below in Figure 13.
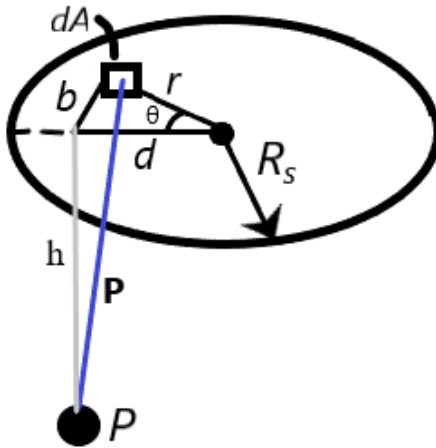
Figure 13: Visualization of flux in the scenario geometry. Path from an infinitesimal section of the planar disk source to point P at a distance "h" below the source and a distance "d" off-center.

The flux at point P in this geometry can be calculated by Equation 11:

$$\varphi_A = \int \frac{S_A}{4\pi P^2} dA \quad (11)$$

Where S_A is the source strength divided by the area of the disk source.

Using the geometry in Figure 13 in conjunction with the law of cosines, it can be seen that:

$$\boldsymbol{P}^2 = h^2 + b^2$$

$$\boldsymbol{P}^2 = h^2 + d^2 + r^2 - 2rd \cos \theta \qquad (12)$$

Substituting Equation 12 into Equation 11 provides the double integral found in Equation 13. This can be solved analytically to determine the integrated flux over the entire area of the disk source (Eq. 14) (Shultis and Faw, 1996).

$$\varphi_A = \int_0^{R_S} \int_0^{2\pi} \frac{S_A * r}{4\pi(h^2 + d^2 + r^2 - 2rd \cos \theta)} d\theta \, dr \qquad (13)$$

$$\varphi_A = \frac{S_A}{4} * \ln \left\{ \frac{R_s^2 + h^2 - d^2 + \sqrt{(R_s^2 + h^2 - d^2)^2 + 4d^2h^2}}{2h^2} \right\} \qquad (14)$$

In this work, the source activity, exposure time, and yield normally associated with the source strength will be accounted for at a different time in the dose calculation. Therefore, the average flux factor will be unitless. Flux was calculated from the entire disk source to ten individual dose points along the dose-disk radius at 0.1 cm increments. Replacing R_s with 1 cm, the average flux factor is explicitly defined in Equation 15, where the integer n represents each of the ten 0.1 cm-increment-dose points to which flux has been calculated along R_{eff}.

$$\varphi = \frac{1}{4\pi n} * \sum_{n=1}^{10} \ln \left\{ \frac{1 + h^2 - (0.1n)^2 + \sqrt{(1 + h^2 - (0.1n)^2)^2 + 4(0.1n)^2 h^2}}{2h^2} \right\}$$

(15)

Excel VBA was used to determine flux at each 0.1 cm increment along R_d as a function of tissue depth using Equation 15. These ten values were averaged to determine the unitless "*average flux" factor, φ*, for each discrete tissue depth.

For the stopping power calculations that will be explained in more detail in section 4.3.5, the analytical dosimetry model treats the source as a point in order to create a sort of "distribution" of stopping power at each discrete tissue depth. When modeled as a point source, the portion of the dose-disk that can be impacted by particles emitted from the source shrinks down to an "effective" dose area. The purpose of the average flux factor is to extrapolate the dose from the "effective" dose area to the entire dose-disk, in the scenario's true disk-disk geometry, after carrying out stopping power calculations in a point source geometry.

4.3.3. Range of ^{212m}Po

To determine what potential tumor depths ^{212m}Po may be able to impact, the range of its alpha particle emissions was determined by using the NCSS fit equation for density range in air (Eq. 8) in combination with the Bragg-Kleeman rule (Eq. 3). The combined equation for range in tissue is shown below (Eq. 16). Atomic weights and densities for tissue, water, and air are summarized in Table 7.

$$\Lambda_{tissue} = \sqrt{\frac{M_{tissue}}{M_{air}\rho_{tissue}}} *$$

$$EXP(\frac{-14.96898-192.5433\sqrt{E}+187.0846E-175.3049(E)^{\frac{3}{2}}+13.24883E^2}{1+23.30342\sqrt{E}-16.47945E+13.72544(E)^{\frac{3}{2}}+3.416341E^2})$$

(16)

Table 7: Atomic mass and density values for air, water, and tissue.

Material	M (g/mol)	ρ (g/cm^3)
Air	14.661	0.0012
Water	14.335	0.998
Tissue	13.991	1.00

The values in Table 7 can be substituted into Eq. 16 along with the 11.66 MeV alpha particle energy, to determine the range of this alpha emission in tissue.

Λ_{tissue}

$$= \sqrt{\frac{13.991}{14.661 * 1.00}}$$

$$* EXP(\frac{-14.96898 - 192.5433\sqrt{11.66} + 187.0846(11.66) - 175.3049(11.66)^{\frac{3}{2}} + 13.24883(11.66)^2}{1 + 23.30342\sqrt{11.66} - 16.47945(11.66) + 13.72544(11.66)^{\frac{3}{2}} + 3.416341(11.66)^2}$$

$= \textbf{165 µm.}$

4.3.4. Tumor depth determinations

After the range of the 11.66 MeV alpha particle in tissue was calculated, three theoretical tumor thicknesses were chosen to study. The three tumor depth ranges that were chosen were 0-50 µm, 0-100 µm, and 0-150 µm, all theoretically traversable by the calculated ^{212m}Po alpha particle range of 165 µm. Because epidermal thickness

varies widely with body site as discussed in section 2.1.2, early-stage NMSC tumors that are confined to the epidermis or have only minimally invaded the dermis would mostly fall into these tissue depth ranges.

To see if additional dosimetry information could be obtained by studying different portions of the tumors, doses to three other cell sizes were also determined: 0-50 µm (Cell 1), 50-100 µm (Cell 2), and 100-150 µm (Cell 3). These cells and tumor depths can be seen schematically in Figure 14. It can be seen that Cell 1 and Tumor 1 have the same dimensions. Cell 2 corresponds to the bottom/deeper half of Tumor 2 or the "middle chunk" of Tumor 3. Cell 3 corresponds to the deepest third of Tumor 3.
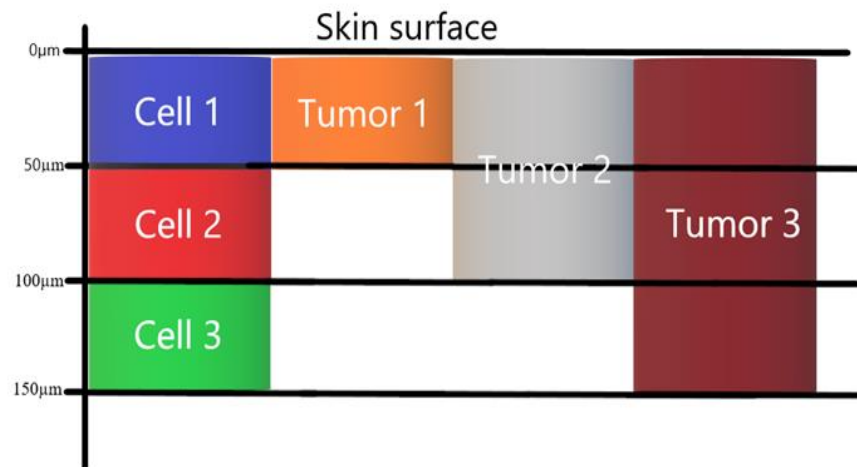
Figure 14: Diagram of individual cells 1, 2, 3, and Tumors 1, 2, 3.

4.3.5. Parameters of mass stopping power calculations

The determination of the mass stopping power of an alpha particle emitted from a disk source to any point on a disk-shaped target is deceptively complicated. Say an arbitrary point P on the dose-disk in Figure 12 is chosen. An alpha particle emitted from a disk source can reach point P by a variety of directions. The travel length

between a source point and dose point P can vary in value between roughly the tissue depth in question and the range of the alpha particles themselves. Point P could be reached from a point "above" on the source disk, leading to a shorter path length, or point P could be reached by an alpha emitted much farther than its translational position in the source plane – say, a particle coming "sideways" from the left edge of the source-disk to the right edge of the dose-disk.

With particle travel length varying to such a degree, it made the most sense to remodel the scenario geometry as a point source-disk target geometry for the sake of mass stopping power determinations. A point source has a specific area at the center of the dose-disk that the emitted particles can impact, which is referred to in this work as the "effective dose area," a dose-disk with an "effective radius." When this effective radius was divided into 10 concentric annuli, path length from the point source to the edge of each annulus could be determined, leading in turn to the determination of residual density range, energy, and therefore stopping power of the particle at the edge of each annulus.

Referencing Figure 12, an alpha particle emitted from a point at the center of the disk source will physically travel less to get to the center of the effective dose area than the particle would travel to get to the edge of the effective dose area. Stopping power for alpha particles increases greatly towards the end of the particles' tracks, as discussed in section 3.1.2. When the effective dose area is divided into ten concentric annuli, and particle travel length from the point source is calculated to the edge of each annulus, it will be seen that the stopping power for each annulus gets subsequently larger, as the particle emitted from the point source is reaching the end of its track.

Stopping power in this scenario starts at lower values towards the center of the effective dose area and becomes larger towards the edge of this area. The average flux factor, in turn, aims to extrapolate the dose profile of the effective radius from the modeled point source to the entire disk-disk geometry.

4.3.5.1. Particle travel length, r_t

The stopping power of alpha particles varies along the particle's track. Due to the short range of alpha particles, and the potential for the dose volume to encompass the end of the alpha track, small differences in particle travel can lead to large variations in stopping power and consequently dose. Therefore, it is more efficient to calculate stopping power from a point source to a smaller "effective" dose area and extrapolate the dose profile of the effective dose area to the entire dose-disk using the average flux factor at the end of the dose calculation. The "effective radius" is the maximum radius the effective dose area can have given the range of the alpha particle and the tissue

depth at which dose is being calculated. This is denoted in Figure 12 as R_{eff}. A more detailed diagram of this geometry is shown below in Figure 15.
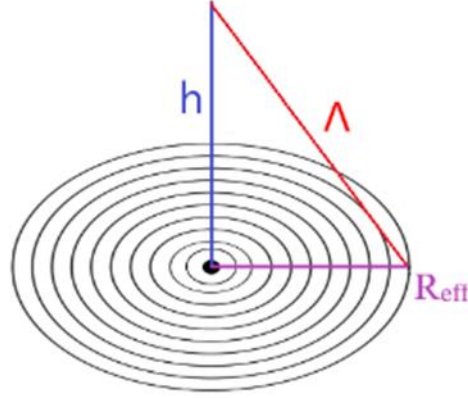
Figure 15: Geometry of the effective radius. In the temporary point source geometry, the effective radius (R_{eff}) is the maximum that can be achieved at that dose depth given the range of the alpha particle in tissue.

From the geometry of Figure 15, it can be seen that (Eq. 17):

$$R_{\text{eff}} = \sqrt{\Lambda^2 - h^2} \qquad (17)$$

where Λ is the energy-specific range of the alpha particles and h is the tissue depth in question.

As the maximum range of the alpha particles coming from the source does not change, R_{eff} depends only on the changing tissue depth. Once the effective radius is established, the radius is divided by ten, creating ten concentric dose circles (annuli) of radii $(\sqrt{\Lambda^2 - h^2})/10$. Figure 15 (above) also shows these dose annuli.

The angle θ from the modeled point source to the outer edge of each annulus can be found by Equation 18:

$$\theta_i = \tan^{-1}\left[(R_{\text{eff},i} + \frac{R_{\text{eff},i} - R_{eff,i-1}}{2}) * \frac{1}{h}\right] \qquad (18)$$

where the integer i ranges from 1-10 and represents each concentric annulus that makes up the effective dose area.

The particle travel length r_t between the source point and the outer edge of an annulus i is then found to be (Eq. 19):

$$r_{t,i} = \frac{h}{\cos\theta_i} \qquad (19)$$

With a definitive path length between source point and dose point established, residual density range and energy, and therefore stopping power and dose, are calculable.

4.3.5.2.　　　Particle energy at dose annulus

After reaching the outer edge of an annulus, the alpha particle will have a residual amount of range (in tissue). The residual density range of the alpha particle at distance r_t can be used to find the energy deposited at this distance. The residual density range can be found using Equation 20:

$$(\Lambda\rho)_{\text{res},i} = (\Lambda - r_{t,i}) * \rho_{tissue} \qquad (20)$$

One of the three fit equations found with NCSS was alpha particle energy as a function of density range (Eq. 9). Substituting the value for residual density range found with Eq. 20, the remaining energy of the alpha particle after traversing length r_t can be found with Eq. 9.

Finally, mass stopping power at the edge of each dose annulus at tissue depth h can be determined using the NCSS fit equation for mass stopping power (Eq. 10).

4.3.6. Annulus weighting

Prior to calculating dose to each annulus, each must be weighted in terms of their area relative to the entire dose-disk which is a disk of radius R_d. This weighting factor is described in Equation 21.

$$w_i = \frac{\pi(R_{\text{eff},i}^2 - R_{\text{eff},i-1}^2)}{\pi R_d^2} \quad (21)$$

4.3.7. Total dose at depth

After the weight of each annulus is calculated using Eq. 21, the dose to each annulus i can be calculated using Eq. 22.

$$\dot{D_i} = \frac{1.6E{-}10\,[\frac{J \cdot g}{MeV \cdot kg}] * (S/\rho)_i\,[\frac{MeV \cdot cm^2}{g}] * w_i}{4\pi r_{t,i}^2\,[cm^2]} * \frac{A\,[dps]}{\lambda\,[s^{-1}]}(1 - \exp(-\lambda\tau)) * Y\left[\frac{alphas}{decay}\right] * w_R\,[\frac{Sv}{Gy}]$$

$$(22)$$

where A is the source activity (in decays/sec) integrated over the exposure time, Y is the radiation yield, τ is the exposure time (in seconds), and w_R is the radiation weighting factor (20 for alpha particles).

Efforts were made to emulate real-world radiation therapy techniques using clinical references from previous beta-emitting skin patch trials. An exposure time of 600 seconds (10 minutes) and an activity of 1.85 MBq (0.05 mCi) were chosen. These values were also chosen to closely approximate the "goal dose" of 40-50 Sv to the largest of the tumor sizes (0-150 μm). These values including that of the "goal dose"

are consistent with the existing literature on radioactive skin patch therapies (Lee et al, 1997; Jeong et al, 2003; Pashezadah, 2019).

After the dose to each annulus is calculated, these can be summed and multiplied by the unitless average flux factor (Eq. 14) for dose to the entire dose-disk at a certain discrete depth (Eq. 23).

$$D = \varphi * \sum_{i=1}^{10} D_i \qquad (23)$$

Recall that the effective radius parameter is created by modeling the source as a point for stopping power calculations. The effective radius essentially creates a "distribution" of stopping power across a portion of the dose-disk (the effective dose area). The average flux factor accounts for the entirety of the source disk and target, with the goal of extrapolating the dose profile from the effective radius, including the "distribution" of stopping powers, to the entire dose-disk in a disk-disk geometry.

4.4. Monte Carlo N Particle Code (MCNP)

Monte Carlo N Particle Code Version 6 (MCNP), a general radiation transport code, was used to calculate dose from alpha particles in a scenario similar to that of the dosimetry model described in section 4.3. While the analytical model presents a volume-averaged method of dose calculations, MCNP determines energy deposition in a cell of interest by calculating the volume or mass of the cell to incorporate into dose calculations.

A 1-cm-radius "infinitely thin" disk source isotropically emitting [212m]Po alpha particles ($E = 11.66$ MeV, $Y = 96.9\%$) was modeled to be directly on the skin surface.

Dose was calculated to cell dimensions identical to those of Cells 1, 2, and 3 used in the analytical model (reference Fig. 14), each modeled as a cylinder. These results were then analyzed to find doses to Tumors 1, 2, and 3. In addition, another run was performed where doses were assessed at 0.1 µm increment tissue depths to create a dose-per-micron depth graph for comparison with the analytical model. This run used the same geometry as the previous run, but dose was assessed to 0.1 µm-thick tissue volumes as opposed to 50 µm thicknesses.

A tally card of *F8:A was used for all dose calculations. This refers to an energy deposition tally for alpha particles with dose results reported in MeV/particle. This tally was used to measure the energy deposited in the volume (or "cell") of interest. The volumes of interest in this model, identical to Cells 1, 2, and 3 from the analytical model, can be viewed as cylinders each with radius equaling 1 cm, bounded by the input cell dimensions for a total volume of roughly 0.016 cm^3 for each cell. Complete specifications for the MCNP parameters that were used in the runs for doses to Cells 1, 2, and 3 can be found in Appendix B.

With the dimensions of the cells laid out, MCNP is also able to calculate the volume and mass of each cell in units of grams and reports these values. Finally, MCNP reports energy deposited to each cell in MeV/particle. Energy deposition in MeV per particle can be converted to dose in Gy per particle by use of Equation 24 below,

$$D\left[\frac{Gy}{particle}\right] = \frac{\varepsilon\left[\frac{MeV}{particle}\right]*1.602E-13\left[\frac{J}{MeV}\right]*1000\left[\frac{g}{kg}\right]}{m_{cell}\,[g]} \qquad (24)$$

where ε is the energy per particle imparted to (deposited in) the cell. m_{cell} is the mass of the cell in grams.

From here, dose is calculated by multiplying the dose per particle by the activity of the source integrated over the exposure time (Eq. 7), the alpha particle yield of the source, and the radiation weighting factor(Eq. 25). Due to the multiplication of dose by a radiation weighting factor, the resultant dose equivalent will be in units of Sv.

$$D\ [Sv] = D\ \left[\frac{Gy}{particle}\right] * \frac{A\ [dps]}{\lambda\ [s^{-1}]}(1 - \exp(-\lambda\tau)) * Y\left[\frac{alphas}{decay}\right] * 20\ \left[\frac{Sv}{Gy}\right] \quad (25)$$

5 Results and Discussion

Results from the analytical dosimetry model described in section 4.3 are compared to MCNP results from the method described in section 4.4.

5.1. Analytical model results

Table 8 shows the results of the dosimetry model described in section 4.3. Using the tumor parameters found in section 4.2.3, doses were calculated to three tumor thicknesses: 0-50 µm or Tumor 1, 0-100 µm or Tumor 2, and 0-150 µm or Tumor 3. These results are found in the fourth column of Table 8. Doses to individual stacked Cells 1 (0-50 µm), 2 (50-100 µm), and 3 (100-150 µm) are found in column 2. (See Figure 14 for a diagram of these cells and tumors.)

Table 8: Results from the analytical dosimetry model described in section 4.3. All doses are given in Sv.

Analytical Results			
Cell Dimensions	Dose to cell (Sv)	"Tumor" max depth	Cumulative dose (Sv)
Cell 1: 0-50 µm	86.8	Tumor 1: 50 µm	86.8
Cell 2: 50-100 µm	33.1	Tumor 2: 100 µm	59.9
Cell 3: 100-150 µm	14.2	Tumor 3: 150 µm	44.7

To calculate the values in Table 8, dose was first determined at 0.1 µm increment depths starting at 0.1 µm directly below skin surface and extending to the end of the alpha particles range (165 µm for the analytical model). After dose was calculated at these 0.1 µm tissue depth increments, doses were averaged across the depth ranges of interest to find doses to Tumors 1-3 and Cells 1-3. The dose to each Cell was the average of 500 doses at discrete depths, while doses to Tumors 1, 2, and 3 were the results of averaging 500, 1000, and 1500 discrete dose depths, respectively.

An outline of the calculational method is provided below, showing partially the intermediate steps of the calculation of dose to Cell 1/Tumor 1, which has dimensions of 0-50 µm. The procedure shown is repeated at 0.1 µm depths from just below the skin surface to the edge of the alpha particles' range. For Tumor 1 and Cell 1, this corresponds to 500 such iterations of this process. Presented here is the calculation of dose at 50 µm tissue depth, the last iteration of the analytical method that factors into the volume-averaged dose calculation for Tumor 1. The first step of the method is to calculate the unitless average flux factor at 50 µm (0.005 cm) using Equation 15:

$$\varphi$$

$$= \frac{1}{4\pi(10)}$$

$$* \sum_{n=1}^{10} \ln\left\{\frac{1 + 0.005^2 - (0.1n)^2 + \sqrt{(1 + 0.005^2 - (0.1n)^2)^2 + 4(0.1n)^2(0.005)^2}}{2(0.005)^2}\right\}$$

$$\Rightarrow \varphi = 0.766$$

This will be used towards the end of the calculation after dose to the effective dose area has been determined. The next step is to find the effective radius (Eq. 17):

$$R_{\text{eff}} = \sqrt{\Lambda^2 - h^2} = \sqrt{0.0165^2 - 0.005^2} = 0.0157 \text{ cm}$$

The value of the effective radius is divided by 10 to get ten equally spaced concentric annuli that make up the effective dose-disk. Each annulus radius is denoted by $r_{\text{eff},i}$ and are listed in the table below. The above value is the effective radius *as well as* the radius of the largest annulus, denoted as $r_{\text{eff},10}$.

Annulus radius	[cm]	Annulus radius	[cm]
$r_{\text{eff},1}$	0.00157	$r_{\text{eff},6}$	0.00943
$r_{\text{eff},2}$	0.00315	$r_{\text{eff},7}$	0.0110
$r_{\text{eff},3}$	0.00472	$r_{\text{eff},8}$	0.0126
$r_{\text{eff},4}$	0.00629	$r_{\text{eff},9}$	0.0142
$r_{\text{eff},5}$	0.00786	$r_{\text{eff},10}$	0.0157

From here, the angle θ_i can be calculated for each annulus using Equation 18. The calculation for the angle θ_{10}, corresponding to annulus radius $r_{\text{eff},10}$, is shown below, and the results of θ_i that correspond to the other nine annuli are presented in the table below.

$$\theta_{10} = \tan^{-1}\left[(0.0157 + \frac{0.0157 - 0.0142}{2}) * \frac{1}{0.005}\right] = 1.25 \text{ radians}$$

θ_i	[radians]	θ_i	[radians]
θ_1	0.156	θ_6	1.05
θ_2	0.441	θ_7	1.12
θ_3	0.666	θ_8	1.17
θ_4	0.833	θ_9	1.21
θ_5	0.956	θ_{10}	1.25

Next, the travel length from the point source to the edge of each annulus, $r_{t,i}$, is found with Equation 19. The calculation of $r_{t,10}$ is shown below, with the values of travel length to the edge of the other nine annuli presented in a table below.

$$r_{t,10} = \frac{0.005}{\cos(1.25)} = .0158$$

$r_{t,i}$	[cm]	$r_{t,i}$	[cm]
$r_{t,1}$	0.00506	$r_{t,6}$	0.00999
$r_{t,2}$	0.00553	$r_{t,7}$	0.0114
$r_{t,3}$	0.00636	$r_{t,8}$	0.0128
$r_{t,4}$	0.00744	$r_{t,9}$	0.0143
$r_{t,5}$	0.00866	$r_{t,10}$	0.0158

With the path length between the modeled point source and the edge of each annulus known, it is possible to determine residual density range (Eq. 20), and therefore residual energy (Eq. 9) and stopping power (Eq. 10) of the alpha particle at the edge of each annulus. Residual density range is calculated at the edge of the largest annulus ($r_{eff,10}$) below, with the values for the other annuli presented in the table below.

$$(\Lambda\rho)_{res,10} = (0.0165 \ [\text{cm}] - 0.0158 \ [cm]) * 1.00 \ [\tfrac{g}{cm^3}] = 7.47\text{E-}4 \ \text{g/cm}^2$$

$(\Lambda\rho)_{res,i}$	[g/cm²]	$(\Lambda\rho)_{res,i}$	[g/cm²]
$(\Lambda\rho)_{res,1}$	0.0114	$(\Lambda\rho)_{res,6}$	0.00651
$(\Lambda\rho)_{res,2}$	0.0110	$(\Lambda\rho)_{res,7}$	0.00512
$(\Lambda\rho)_{res,3}$	0.0102	$(\Lambda\rho)_{res,8}$	0.00369
$(\Lambda\rho)_{res,4}$	0.00906	$(\Lambda\rho)_{res,9}$	0.00223
$(\Lambda\rho)_{res,5}$	0.00784	$(\Lambda\rho)_{res,10}$	0.000747

The values of residual density range in the above table can be plugged into Equation 9, copied below for convenience, to get the residual energy at the edge of each annulus. Values of residual energy for each annulus can be found in the table below.

$$E = \frac{-3.447587 - 1.248744(\ln(\Lambda\rho_{air})) - 0.1711394(\ln(\Lambda\rho_{air}))^2 - 0.01046125(\ln(\Lambda\rho_{air}))^3 - 30.06026(\ln(\Lambda\rho_{air}))^4}{1 + 1.047572(\ln(\Lambda\rho_{air})) + 0.4176743(\ln(\Lambda\rho_{air}))^2 + 0.08294695(\ln(\Lambda\rho_{air}))^3 + 0.008196484(\ln(\Lambda\rho_{air}))^4 - 0.0003223555(\ln(\Lambda\rho_{air}))^5} \tag{9}$$

E_i	[MeV]	E_i	[MeV]

E_1	9.22	E_6	6.49
E_2	8.99	E_7	5.55
E_3	8.57	E_8	4.45
E_4	8.00	E_9	3.12
E_5	7.30	E_{10}	1.14

The stopping power can then be calculated at the edge of each annulus by plugging the values of residual energy from the previous table into Equation 10, copied below for convenience. The values for stopping power at the edge of each annulus are found in the table below.

$$\frac{S}{\rho} =$$

$$\frac{2187.7 - 2.57008(\ln E) + 942.6795(\ln E)^2 + 7.422102(\ln E)^3 - 30.06026(\ln E)^4 - 4.952705(\ln E)^5}{1 + 0.2338179(\ln E) + 0.8293901(\ln E)^2 + 0.1650164(\ln E)^3 + 0.1138328(\ln E)^4 - 0.005094198(\ln E)^5}$$

(10)

$(\frac{S}{\rho})_i$	[MeV·cm²·g⁻¹]	$(\frac{S}{\rho})_i$	[MeV·cm²·g⁻¹]
$(\frac{S}{\rho})_1$	565.2	$(\frac{S}{\rho})_6$	728.6
$(\frac{S}{\rho})_2$	575.8	$(\frac{S}{\rho})_7$	813.5

$$\left(\frac{S}{\rho}\right)_3 \quad 596.5 \qquad \left(\frac{S}{\rho}\right)_8 \quad 947.5$$

$$\left(\frac{S}{\rho}\right)_4 \quad 627.2 \qquad \left(\frac{S}{\rho}\right)_9 \quad 1205.3$$

$$\left(\frac{S}{\rho}\right)_5 \quad 669.7 \qquad \left(\frac{S}{\rho}\right)_{10} \quad 2106.5$$

One will notice that the stopping power increases dramatically as the particle reaches the edge of the effective radius. This is what would be expected, as alpha particles deposit the majority of their energy at the end of their tracks.

The weight of each annulus is found by using Equation 21, which compares the area of the annulus to the area of the entire dose-disk. The weight of the largest annulus ($r_{eff,10}$) is calculated below, with the weight of the rest of the annuli presented in table form.

$$w_{10} = \frac{\pi(0.0157^2 - 0.0142^2)}{\pi(1)^2} = 4.7E-5$$

w_i	[unitless]	w_i	[unitless]
w_1	2.45E-6	w_6	2.72E-5
w_2	7.42E-6	w_7	3.21E-5
w_3	1.24E-5	w_8	3.71E-5
w_4	1.73E-5	w_9	4.20E-5
w_5	2.23E-5	w_{10}	4.70E-5

The dose to each annulus that makes up the effective dose area can be found with Equation 22. The dose to the largest annulus is calculated below, with doses to the other annuli presented in a table below.

$$\dot{D}_\iota \, [Sv] = \frac{1.6E-10 \left[\frac{J \cdot g}{MeV \cdot kg}\right] * (S/\rho)_i \left[\frac{MeV \cdot cm^2}{g}\right] * w_i}{4\pi r_t^2 \, [cm^2]}$$

$$* \frac{A \, [dps]}{\lambda \, [s^{-1}]} (1 - \exp(-\lambda\tau)) * Y \left[\frac{alphas}{decay}\right] * 20 \, [\frac{Sv}{Gy}]$$

$$\dot{D}_{10} = \frac{(1.602E-10) * 2106.5 * 4.7E-5}{4\pi(0.0158)^2} * \frac{1.85E6}{0.0154} (1 - \exp(-0.0154 * 600))$$

$$* 0.969 * 20$$

$\Rightarrow \dot{D}_{10} = 11.8 \, Sv$

D_i	[Sv]	D_i	[Sv]
D_1	1.62	D_6	5.89
D_2	4.15	D_7	5.99
D_3	5.41	D_8	6.36
D_4	5.83	D_9	7.38
D_5	5.89	D_{10}	11.8

The above table lists the dose to each annulus that makes up the effective dose area. Finally, for the total dose to the entire infinitely thin dose-disk at 50 µm below skin

surface, the ten annuli doses are summed and multiplied by the average flux factor (Eq. 23).

$$D \ = 0.766 * \sum_{i=1}^{10} D_i \ = 46.2 \text{ Sv}$$

As mentioned previously, finding total dose to Tumor 1 relies on 500 runs of the above calculational steps at 0.1 μm tissue depth increments, and averages them to find a "volume-averaged" dose to the tumor. Doses to Tumors 2 and 3 therefore rely on a greater number of depths to be averaged, 1000 and 1500, respectively. Below are the dose results for the 500 discrete tissue depths that were averaged to get the dose to Tumor 1, each at 0.1 μm increments beginning at 0.1 μm below skin surface and extending to 50 μm, corresponding to the dimensions of Tumor 1.

Tissue depth h [cm]	Σ D [Sv]	φ	φ*Σ D [Sv]	Tissue depth h [cm]	Σ D [Sv]	φ	φ*Σ D [Sv]	Tissue depth h [cm]	Σ D [Sv]	φ	φ*Σ D [Sv]	Tissue depth h [cm]	Σ D [Sv]	φ	φ*Σ D [Sv]	Tissue depth h [cm]	Σ D [Sv]	φ	φ*Σ D [Sv]
0.00001	151.975483	1.705635	259.214636	0.00101	113.1869	1.007846	114.074889	0.00201	89.78987	0.903799	81.1520187	0.00301	76.87304	0.842751	64.78482645	0.00401	67.64398	0.799386	54.07336839
0.00002	151.949	1.600833	243.244485	0.00102	112.8395	1.006356	113.556703	0.00202	89.62936	0.903049	80.939695	0.00302	76.76718	0.842249	64.65711913	0.00402	67.56291	0.799001	53.9834389
0.00003	151.904279	1.539528	233.860821	0.00103	112.4955	1.004881	113.044555	0.00203	89.46967	0.902302	80.7286907	0.00303	76.66166	0.84175	64.52992676	0.00403	67.482	0.798634	53.8934477
0.00004	151.842	1.496031	227.16041	0.00104	112.1548	1.00342	112.53834	0.00204	89.31088	0.901559	80.5190582	0.00304	76.5565	0.841252	64.40327606	0.00404	67.4013	0.798261	53.8037425
0.00005	151.762247	1.462292	221.920753	0.00105	111.8173	1.001973	112.037971	0.00205	89.15294	0.90082	80.3107593	0.00305	76.45162	0.840755	64.27709238	0.00405	67.32076	0.797886	53.714292
0.00006	151.665	1.434726	217.597756	0.00106	111.4831	1.00054	111.543347	0.00206	88.99584	0.900084	80.1037629	0.00306	76.34713	0.84026	64.15145686	0.00406	67.24039	0.797513	53.6251018
0.00007	151.550489	1.411419	213.901184	0.00107	111.1521	0.999121	111.054395	0.00207	88.83956	0.899352	79.8980616	0.00307	76.24291	0.839767	64.02628265	0.00407	67.16022	0.797141	53.5361891
0.00008	151.419	1.391229	210.658316	0.00108	110.8243	0.997714	110.570995	0.00208	88.68412	0.898624	79.6936461	0.00308	76.13905	0.839275	63.90163115	0.00408	67.0802	0.79677	53.4475128
0.00009	151.270295	1.373421	207.757751	0.00109	110.4996	0.996321	110.093065	0.00209	88.5295	0.897899	79.4905095	0.00309	76.03552	0.838785	63.77747951	0.00409	67.00036	0.7964	53.3591117
0.0001	151.105	1.357491	205.12373	0.0011	110.178	0.99494	109.620522	0.0021	88.37567	0.897177	79.2886067	0.0031	75.9323	0.838297	63.65381304	0.0041	66.92071	0.796031	53.270968
0.00011	150.923467	1.34308	202.702278	0.00111	109.8595	0.993572	109.153276	0.00211	88.22268	0.896459	79.0879857	0.00311	75.8294	0.83781	63.53062593	0.00411	66.8412	0.795663	53.1830611
0.00012	150.726	1.329924	200.453772	0.00112	109.544	0.992216	108.691309	0.00212	88.0704	0.895744	78.8885142	0.00312	75.72681	0.837325	63.40793024	0.00412	66.76189	0.795296	53.0954318
0.00013	150.512202	1.317822	198.348274	0.00113	109.2315	0.990872	108.234423	0.00213	87.91896	0.895032	78.6903121	0.00313	75.62452	0.836841	63.28569305	0.00413	66.68276	0.794929	53.008065
0.00014	150.283	1.306617	196.362671	0.00114	108.922	0.98954	107.782628	0.00214	87.76826	0.894324	78.4932848	0.00314	75.5226	0.836359	63.16398236	0.00414	66.60377	0.794564	52.920928
0.00015	150.039239	1.296186	194.47869	0.00115	108.6154	0.988219	107.335797	0.00215	87.61833	0.893619	78.2974394	0.00315	75.42094	0.835878	63.04270373	0.00415	66.52495	0.794199	52.8340365
0.00016	149.780	1.286428	192.681666	0.00116	108.3116	0.98691	106.893856	0.00216	87.46914	0.892918	78.1027571	0.00316	75.31961	0.835399	62.92191613	0.00416	66.44633	0.793835	52.7474239
0.00017	149.507286	1.277261	190.959868	0.00117	108.0107	0.985612	106.45672	0.00217	87.32073	0.89222	77.9092637	0.00317	75.21859	0.834921	62.80159315	0.00417	66.36783	0.793472	52.6610178
0.00018	149.220	1.268619	189.303585	0.00118	107.7127	0.984326	106.024321	0.00218	87.173	0.891524	77.7168583	0.00318	75.11783	0.834445	62.68170085	0.00418	66.28954	0.79311	52.5748919
0.00019	148.919582	1.260444	187.704848	0.00119	107.4173	0.98305	105.596578	0.00219	87.02605	0.890833	77.525632	0.00319	75.01742	0.83397	62.56304461	0.00419	66.21142	0.792749	52.4890229
0.0002	148.606	1.252689	186.156944	0.0012	107.1247	0.981785	105.173413	0.0022	86.87978	0.890144	77.3354912	0.0032	74.91731	0.833497	62.44336603	0.0042	66.13343	0.792388	52.4033643
0.00021	148.279533	1.245312	184.654297	0.00121	106.8349	0.98053	104.754775	0.00221	86.73424	0.889458	77.1464714	0.00321	74.81748	0.833026	62.32486608	0.00421	66.05561	0.792029	52.3179521
0.00022	147.941	1.238278	183.192129	0.00122	106.5477	0.979285	104.340573	0.00222	86.5894	0.888776	76.958546	0.00322	74.71794	0.832555	62.20681646	0.00422	65.97795	0.79167	52.2327833
0.00023	147.590727	1.231558	181.766468	0.00123	106.2631	0.978051	103.930732	0.00223	86.44525	0.888096	76.7716862	0.00323	74.61872	0.832087	62.08922829	0.00423	65.90045	0.791312	52.1478506
0.00024	147.229	1.225123	180.37375	0.00124	105.9811	0.976827	103.525201	0.00224	86.30178	0.88742	76.5858917	0.00324	74.51975	0.831619	61.97205697	0.00424	65.82311	0.790956	52.0631544
0.00025	146.856814	1.218951	179.011191	0.00125	105.7016	0.975613	103.123839	0.00225	86.159	0.886746	76.4011649	0.00325	74.42109	0.831153	61.8553408	0.00425	65.74596	0.790599	51.978718
0.00026	146.474	1.213021	177.67611	0.00126	105.4247	0.974408	102.72666	0.00226	86.0169	0.886076	76.2174875	0.00326	74.32275	0.830689	61.73908147	0.00426	65.66896	0.790244	51.8945103
0.00027	146.081641	1.207314	176.366457	0.00127	105.1503	0.973213	102.333636	0.00227	85.87547	0.885408	76.0348492	0.00327	74.22467	0.830226	61.62324343	0.00427	65.59207	0.78989	51.8105012
0.00028	145.680	1.201816	175.080252	0.00128	104.8783	0.972027	101.944553	0.00228	85.73465	0.884744	75.8531986	0.00328	74.12686	0.829764	61.50781555	0.00428	65.51539	0.789536	51.726767
0.00029	145.269019	1.19651	173.815835	0.00129	104.6088	0.97085	101.559438	0.00229	85.59457	0.884082	75.6726293	0.00329	74.02935	0.829304	61.39284197	0.00429	65.43886	0.789183	51.6432604
0.0003	144.850	1.191384	172.571834	0.0013	104.3416	0.969683	101.178238	0.0023	85.45506	0.883423	75.4929913	0.0033	73.93209	0.828845	61.27825888	0.0043	65.36247	0.788831	51.559967
0.00031	144.422813	1.186427	171.347059	0.00131	104.0768	0.968524	100.80086	0.00231	85.31622	0.882767	75.3143857	0.00331	73.83512	0.828388	61.16411578	0.00431	65.28627	0.78848	51.476936
0.00032	143.988	1.181626	170.140321	0.00132	103.8143	0.967374	100.427256	0.00232	85.178	0.882114	75.1367369	0.00332	73.73844	0.827932	61.05040142	0.00432	65.21019	0.78813	51.394102
0.00033	143.54679	1.176974	168.9508	0.00133	103.554	0.966233	100.057363	0.00233	85.0404	0.881464	74.960062	0.00333	73.64205	0.827477	60.93711359	0.00433	65.13428	0.78778	51.3115089
0.00034	143.099	1.17246	167.777554	0.00134	103.2961	0.965101	99.6911288	0.00234	84.90346	0.880817	74.7843845	0.00334	73.54589	0.827024	60.82420495	0.00434	65.05849	0.787432	51.2291206
0.00035	142.644704	1.168077	166.620039	0.00135	103.0403	0.963977	99.3284795	0.00235	84.76712	0.880172	74.6096408	0.00335	73.45002	0.826572	60.71172151	0.00435	64.98289	0.787084	51.1469753
0.00036	142.185	1.163818	165.477452	0.00136	102.7867	0.962861	98.9693471	0.00236	84.63134	0.87953	74.4357989	0.00336	73.35443	0.826121	60.59965417	0.00436	64.90744	0.786737	51.0650605
0.00037	141.720133	1.159675	164.349348	0.00137	102.5353	0.961753	98.6136967	0.00237	84.49622	0.878891	74.2629443	0.00337	73.25909	0.825672	60.48798644	0.00437	64.83214	0.786045	50.9833721
0.00038	141.251	1.155643	163.235217	0.00138	102.286	0.960654	98.2614402	0.00238	84.36168	0.878254	74.0909955	0.00338	73.16401	0.825224	60.3767076	0.00438	64.75697	0.786045	50.9018859
0.00039	140.776648	1.151716	162.134699	0.00139	102.0388	0.959562	97.9126182	0.00239	84.2477	0.87762	73.9199361	0.00339	73.06924	0.824778	60.26587042	0.00439	64.68195	0.7857	50.8206119
0.0004	140.299	1.147888	161.04729	0.0014	101.7937	0.958478	97.567031	0.0024	84.0943	0.876989	73.7497819	0.0034	72.97468	0.824332	60.15538471	0.0044	64.60707	0.785356	50.7395637
0.00041	139.817474	1.144155	159.972795	0.00141	101.5506	0.957402	97.2247621	0.00241	83.96149	0.87636	73.5805283	0.00341	72.88043	0.823888	60.04532622	0.00441	64.53238	0.785013	50.6587564
0.00042	139.333	1.140511	158.910889	0.00142	101.3095	0.956334	96.8857309	0.00242	83.82927	0.875734	73.4121751	0.00342	72.78638	0.823446	59.93561981	0.00442	64.45783	0.784671	50.5781628
0.00043	138.845877	1.136953	157.861289	0.00143	101.0704	0.955273	96.5498292	0.00243	83.69764	0.875111	73.2447243	0.00343	72.69262	0.823004	59.82633432	0.00443	64.38337	0.784329	50.4977475
0.00044	138.356	1.133477	156.82382	0.00144	100.8332	0.954219	96.2170135	0.00244	83.56662	0.87449	73.078089	0.00344	72.59912	0.822564	59.71742669	0.00444	64.3091	0.783988	50.417572
0.00045	137.864856	1.13008	155.798273	0.00145	100.598	0.953173	95.88728	0.00245	83.43596	0.873872	72.9123232	0.00345	72.50587	0.822125	59.60890782	0.00445	64.23499	0.783648	50.337627
0.00046	137.372	1.126757	154.784432	0.00146	100.3646	0.952134	95.5605564	0.00246	83.30598	0.873256	72.7474382	0.00346	72.41284	0.821688	59.50074042	0.00446	64.161	0.783309	50.2578708
0.00047	136.877127	1.123505	153.782129	0.00147	100.1331	0.951102	95.2367926	0.00247	83.17652	0.872643	72.5833736	0.00347	72.3201	0.821251	59.39298864	0.00447	64.08713	0.78297	50.1783113
0.00048	136.382	1.120322	152.791291	0.00148	99.90349	0.950077	94.9159788	0.00248	83.04757	0.872032	72.4201189	0.00348	72.22761	0.820816	59.28560262	0.00448	64.01346	0.782632	50.0990103
0.00049	135.885399	1.117204	151.811743	0.00149	99.67564	0.949059	94.5980224	0.00249	82.9192	0.871423	72.2577009	0.00349	72.13536	0.820383	59.17859692	0.00449	63.93988	0.782295	50.0198703
0.0005	135.389	1.11415	150.843342	0.0015	99.44958	0.948047	94.2829117	0.0025	82.79134	0.870817	72.0961447	0.0035	72.04332	0.81995	59.07192712	0.0045	63.86648	0.781959	49.9409749
0.00051	134.892012	1.11116	149.886018	0.00151	99.22529	0.947043	93.9705901	0.00251	82.664	0.870214	71.9353627	0.00351	71.95158	0.819519	58.96567241	0.00451	63.79319	0.781624	49.8622583
0.00052	134.395395	1.10822	148.939626	0.00152	99.00272	0.946045	93.6610087	0.00252	82.53623	0.869613	71.7754247	0.00352	71.86006	0.819089	58.85975852	0.00452	63.72006	0.78129	49.783766
0.00053	133.899172	1.10534	148.004073	0.00153	98.78185	0.945053	93.3541255	0.00253	82.41089	0.869014	71.6162221	0.00353	71.76877	0.81866	58.75420868	0.00453	63.64705	0.780955	49.7054598
0.00054	133.403616	1.102514	147.079297	0.00154	98.56269	0.944068	93.0499221	0.00254	82.28514	0.868418	71.4578691	0.00354	71.6777	0.818232	58.64901135	0.00454	63.57419	0.780621	49.6273696
0.00055	132.908925	1.099739	146.165164	0.00155	98.34515	0.94309	92.7483173	0.00255	82.15983	0.867824	71.3002411	0.00355	71.5869	0.817806	58.54417723	0.00455	63.50146	0.780289	49.5494728
0.00056	132.415403	1.097015	145.261679	0.00156	98.12929	0.942118	92.4493254	0.00256	82.03506	0.867232	71.1434203	0.00356	71.49633	0.81738	58.43970273	0.00456	63.42886	0.779957	49.4717764
0.00057	131.923136	1.094339	144.368618	0.00157	97.91499	0.941152	92.1528435	0.00257	81.91076	0.866643	70.9873463	0.00357	71.40601	0.816956	58.33560176	0.00457	63.35644	0.779626	49.3943118
0.00058	131.432378	1.091709	143.485956	0.00158	97.70235	0.940192	91.8589224	0.00258	81.78697	0.866055	70.8320466	0.00358	71.31589	0.816534	58.23182004	0.00458	63.28411	0.779295	49.3170114
0.00059	130.943345	1.089125	142.61364	0.00159	97.4912	0.939238	91.5674143	0.00259	81.66366	0.865471	70.6774963	0.00359	71.22604	0.816112	58.12841852	0.00459	63.21194	0.778966	49.2399313
0.0006	130.45618	1.086584	141.751548	0.0016	97.28164	0.93829	91.2783663	0.0026	81.54083	0.864888	70.5236804	0.0036	71.13639	0.815691	58.02534189	0.0046	63.1399	0.778637	49.163045
0.00061	129.971095	1.084084	140.899647	0.00161	97.0736	0.937348	90.9917279	0.00261	81.41846	0.864308	70.3705921	0.00361	71.04698	0.815272	57.92261788	0.00461	63.06801	0.778308	49.0863652
0.00062	129.488195	1.081626	140.057795	0.00162	96.86706	0.936412	90.7074426	0.00262	81.29661	0.863729	70.2182811	0.00362	70.9578	0.814854	57.82023876	0.00462	62.99622	0.777981	49.0098545
0.00063	129.007631	1.079207	139.225914	0.00163	96.66198	0.935481	90.4254671	0.00263	81.17518	0.863154	70.0666447	0.00363	70.86885	0.814437	57.7182018	0.00463	62.92457	0.777654	48.9335454
0.00064	128.529593	1.076826	138.403975	0.00164	96.45841	0.934557	90.1458371	0.00264	81.05427	0.86258	69.9157747	0.00364	70.78011	0.814021	57.61648907	0.00464	62.85307	0.777328	48.8574428
0.00065	128.054128	1.074482	137.591805	0.00165	96.25622	0.933637	89.8684178	0.00265	80.93377	0.862008	69.7655776	0.00365	70.69163	0.813606	57.51514921	0.00465	62.78167	0.777002	48.7815155
0.00066	127.581446	1.072173	136.789414	0.00166	96.05551	0.932724	89.593272	0.00266	80.81372	0.861439	69.6160724	0.00366	70.60333	0.813193	57.41410372	0.00466	62.71042	0.776678	48.7057833
0.00067	127.111581	1.0699	135.996632	0.00167	95.85615	0.931816	89.3202824	0.00267	80.69405	0.860872	69.4672964	0.00367	70.51528	0.81278	57.31341837	0.00467	62.63932	0.776354	48.6302663
0.00068	126.644603	1.06766	135.213333	0.00168	95.65819	0.930913	89.0494783	0.00268	80.57504	0.860306	69.3192188	0.00368	70.4274	0.812369	57.21302082	0.00468	62.5683	0.77603	48.5548973
0.00069	126.180752	1.065452	134.439586	0.00169	95.46159	0.930016	88.7808111	0.00269	80.45638	0.859743	69.1718349	0.00369	70.3398	0.811959	57.11299969	0.00469	62.49743	0.775708	48.4797377
0.0007	125.719974	1.063277	133.675146	0.0017	95.26633	0.929124	88.5142417	0.0027	80.33814	0.859182	69.0251121	0.0037	70.25239	0.811549	57.01328116	0.0047	62.42672	0.775386	48.4047868
0.00071	125.262435	1.061132	132.920013	0.00171	95.07238	0.928237	88.249731	0.00271	80.22033	0.858623	68.8790536	0.00371	70.16518	0.811141	56.91388487	0.00471	62.35611	0.775064	48.3300034
0.00072	124.808166	1.059018	132.174051	0.00172	94.87974	0.927356	87.9872707	0.00272	80.10294	0.858067	68.7336782	0.00372	70.07825	0.810734	56.81485156	0.00472	62.2856	0.774744	48.2553837
0.00073	124.357197	1.056932	131.437123	0.00173	94.68839	0.926479	87.7268328	0.00273	79.98606	0.857512	68.5889911	0.00373	69.99147	0.810329	56.71609585	0.00473	62.21527	0.774424	48.1809953
0.00074	123.909637	1.054875	130.709189	0.00174	94.49832	0.925608	87.468387	0.00274	79.86952	0.856959	68.4449119	0.00374	69.9049	0.809924	56.61765136	0.00474	62.14504	0.774105	48.1067677
0.00075	123.465531	1.052846	129.990143	0.00175	94.30948	0.924741	87.2118886	0.00275	79.75345	0.856408	68.3015168	0.00375	69.81859	0.80952	56.51956105	0.00475	62.07494	0.773786	48.0327286
0.00076	123.024931	1.050843	129.27989	0.00176	94.12191	0.92388	86.9573486	0.00276	79.63777	0.855586	68.1587425	0.00376	69.73247	0.809118	56.42177075	0.00476	62.00499	0.773468	47.958888
0.00077	122.587825	1.048867	128.578275	0.00177	93.93553	0.923023	86.704696	0.00277	79.52255	0.855313	68.0166547	0.00377	69.64652	0.808716	56.32426656	0.00477	61.9351	0.773151	47.8851836
0.00078	122.154336	1.046916	127.88529	0.00178	93.75034	0.922172	86.4539084	0.00278	79.40773	0.854768	67.8751844	0.00378	69.5608	0.808316	56.22708173	0.00478	61.86537	0.772834	47.8116867
0.00079	121.724388	1.04499	127.200722	0.00179	93.56639	0.921325	86.2050188	0.00279	79.29327	0.854225	67.734302	0.00379	69.47529	0.807916	56.13021943	0.00479	61.79575	0.772519	47.738361
0.0008	121.298126	1.043088	126.524595	0.0018	93.38358	0.920482	85.9579377	0.0028	79.17928	0.853684	67.5941067	0.0038	69.39002	0.807518	56.03368627	0.0048	61.7263	0.772203	47.6652548
0.00081	120.87544	1.04121	125.856668	0.00181	93.20195	0.919645	85.712688	0.00281	79.06563	0.853145	67.45447354	0.00381	69.30493	0.807121	55.93743869	0.00481	61.65691	0.771889	47.5922745
0.00082	120.456447	1.039354	125.196942	0.00182	93.02142	0.918812	85.4691791	0.00282	78.95242	0.852608	67.3154845	0.00382	69.22001	0.806724	55.84251566	0.00482	61.58766	0.771575	47.5194385
0.00083	120.041152	1.037522	124.545307	0.00183	92.84202	0.917983	85.2274293	0.00283	78.83961	0.852073	67.1771106	0.00383	69.13532	0.806329	55.7458276	0.00483	61.51857	0.771261	47.4468996
0.00084	119.629484	1.035711	123.901578	0.00184	92.66377	0.917159	84.9874526	0.00284	78.72718	0.851539	67.0393276	0.00384	69.05083	0.805935	55.65047685	0.00484	61.44957	0.770949	47.374474
0.00085	119.221532	1.033922	123.265735	0.00185	92.48655	0.91634	84.74913	0.00285	78.61517	0.851008	66.9021719	0.00385	68.96652	0.805542	55.55541304	0.00485	61.3807	0.770637	47.3022291
0.00086	118.817225	1.032153	122.637602	0.00186	92.31047	0.915525	84.5125449	0.00286	78.50348	0.850479	66.7655526	0.00386	68.88243	0.80515	55.46066333	0.00486	61.31193	0.770325	47.2301408
0.00087	118.4166	1.030405	122.017113	0.00187	92.13542	0.914714	84.27759	0.00287	78.39218	0.849951	66.6295331	0.00387	68.79854	0.804759	55.36620858	0.00487	61.24327	0.770015	47.1582259
0.00088	118.019668	1.028678	121.404181	0.00188	91.96147	0.913908	84.0443243	0.00288	78.28135	0.849425	66.4941628	0.00388	68.71483	0.804368	55.27203951	0.00488	61.17474	0.769705	47.0864858
0.00089	117.626389	1.026969	120.798669	0.00189	91.78852	0.913106	83.8126444	0.00289	78.1708	0.848901	66.3592996	0.00389	68.63131	0.803979	55.17815726	0.00489	61.10632	0.769395	47.0149182
0.0009	117.236785	1.02528	120.200507	0.0019	91.61661	0.912308	83.5825813	0.0029	78.06069	0.848379	66.2250613	0.0039	68.54801	0.803591	55.08457796	0.0049	61.03805	0.769086	46.9435402
0.00091	116.8508	1.023609	119.609546	0.00191	91.44574	0.911514	83.3541154	0.00291	77.95088	0.847859	66.0913387	0.00391	68.46487	0.803204	54.99126261	0.00491	60.96986	0.768778	46.8723037
0.00092	116.468449	1.021957	119.025716	0.00192	91.27584	0.910725	83.1271913	0.00292	77.84148	0.84734	65.9582136	0.00392	68.38195	0.802818	54.89826054	0.00492	60.9018	0.768471	46.8012489
0.00093	116.089748	1.020322	118.448947	0.00193	91.10696	0.90994	82.9018295	0.00293	77.73248	0.846823	65.8255698	0.00393	68.29919	0.802433	54.80550915	0.00493	60.83386	0.768164	46.7303713
0.00094	115.714569	1.018705	117.879028	0.00194	90.93902	0.909158	82.6779596	0.00294	77.62379	0.846308	65.693652	0.00394	68.21665	0.802049	54.71307194	0.00494	60.76604	0.767858	46.6596368
0.00095	115.342993	1.017105	117.315959	0.00195	90.77205	0.908381	82.4556006	0.00295	77.51551	0.845795	65.5622162	0.00395	68.13428	0.801665	54.62089593	0.00495	60.6983	0.767552	46.5890954
0.00096	114.974896	1.015522	116.75954	0.00196	90.60603	0.907608	82.2347217	0.00296	77.40754	0.845283	65.4312931	0.00396	68.05209	0.801283	54.52899666	0.00496	60.6307	0.767247	46.5187077
0.00097	114.61037	1.013955	116.209787	0.00197	90.44098	0.906838	82.0153368	0.00297	77.29994	0.844735	65.3009283	0.00397	67.9701	0.800902	54.43789329	0.00497	60.56319	0.766942	46.4484772
0.00098	114.249337	1.012405	115.666548	0.00198	90.27682	0.906073	81.7973641	0.00298	77.19271	0.844265	65.171119	0.00398	67.88831	0.800522	54.34606055	0.00498	60.4958	0.766639	46.3784123
0.00099	113.89176	1.01087	115.129717	0.00199	90.11359	0.905311	81.5808332	0.00299	77.08583	0.843759	65.041844	0.00399	67.80669	0.800142	54.25499991	0.00499	60.42855	0.766335	46.3085334
0.001	113.537588	1.00935	114.59917	0.002	89.95131	0.904553	81.365749	0.003	76.97925	0.843254	64.9130601	0.004	67.72527	0.799764	54.16422576	0.005	60.36139	0.766033	46.2388

Dose to Tumor 1 (average of all bold numbers): 86.8 Sv
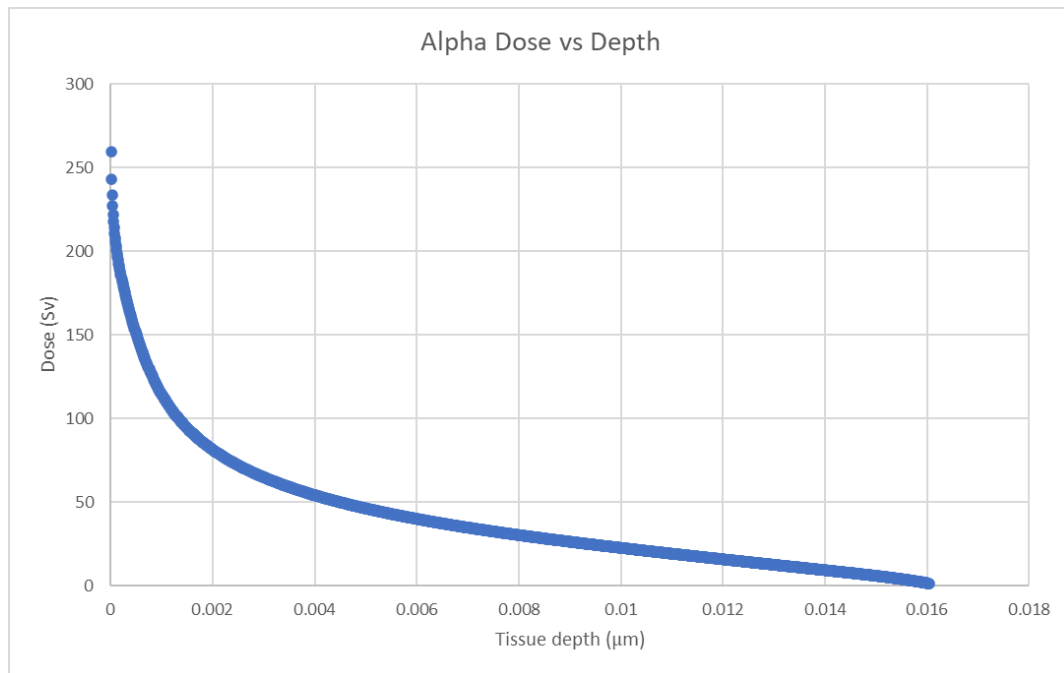
5.1.1. Dose per depth

Figure 16: Dose (Sv) per tissue depth (µm) results for ^{212m}Po alpha particles using the dosimetry model described in Section 4.3.

A graph showing the dose per tissue skin depth (in µm) is found in Figure 16. This graph shows the individual dose received to the 1-cm-radius dose-disk at discrete 0.1 µm increment tissue depths, beginning 0.1 µm below the skin surface and extending to the end of the alpha particles' range. These are the individual discrete doses before they are averaged to find the total doses to Tumors and Cells 1-3.

5.2. MCNP results

The "raw" energy deposition results in MeV/particle from the MCNP simulation for Cells 1, 2, and 3, along with the masses of the cells and error fractions

associated with each energy deposition can be found in Table 9. These results were analyzed to get the doses to Tumors 1-3.

Table 9: MCNP raw results for the main cells (Cells 1, 2, and 3) and the concentric annular volumes surrounding the geometry.

Separated Doses	Main Cells		
Cell Depth Range	Cell Mass (g)	Main Cell Dose(MeV/particle)	Error fraction
0-50 μm	1.57E-02	3.64E+00	0.0002
50-100 μm	1.57E-02	1.76E+00	0.0003
100-150 μm	1.57E-02	3.78E-01	0.0006

Table 10 displays the MCNP dose results from the geometry described in section 4.4. These values were obtained by converting the values in Table 9 to dose using Equations 24 and 25. The cell and tumor depth conventions described as applied to Table 8 also apply to Table 10.

Table 10: MCNP results using the method described in Section 4.4.

MCNP Results			
Cell Dimensions	Dose to cell (Sv)	"Tumor" max depth	Cumulative dose (Sv)
Cell 1: 0-50 μm	86.4 ± 1.66	Tumor 1: 50 μm	86.4 ± 1.66
Cell 2: 50-100 μm	41.9 ± 1.19	Tumor 2: 100 μm	64.0 ± 2.31
Cell 3: 100-150 μm	8.99 ± 0.48	Tumor 3: 150 μm	45.6 ± 3.17

The raw results from Table 9 are converted to the doses in Table 10 via Equations 24 and 25. To demonstrate the use of this equation, an outline is provided below of the conversion of the MCNP output result (App. B) of the energy deposited in Cell 1 (Tumor 1) to the dose in Sv found in Table 10.

```
8-        c Main Cells
9-        11    1        -1      -11   12    -4      IMP:A=1
10-       12    1        -1      -12   13    -4      IMP:A=1
11-       13    1        -1      -13   14    -4      IMP:A=1

22-       c Surfaces

26-       4          cy   1
30-       11         py       0
31-       12         py       -0.005
32-       13         py       -0.01
33-       14         py       -0.015
```

The values in Line 9 (red box above) describe a cylinder of 1-cm radius which extends from 0 cm to 0.005 cm below the surface of the skin. These dimensions correspond to those of Cell 1/Tumor 1 described in this work. MCNP will tally the energy deposited within the cylinder described by these dimensions (referred to internally as "cell 11" in this MCNP run).

```
                     atom      gram                                        alpha
       cell    mat  density   density    volume       mass        pieces importance
  5    11       1  9.58192E-02 1.00000E+00 1.57080E-02 1.57080E-02    1  1.0000E+00


1tally      8      nps =    30000000
       tally type 8*   energy deposition                    units   mev
       particle(s): alphas
cell  11
           3.63633E+00 0.0002
```

After performing the run, MCNP outputs various parameters about each tallied area. MCNP determines the mass of the cell to be 0.0157 g and the energy deposited per particle to be 3.64 MeV with an error of ±0.02%, or ±0.07 MeV. This output provides all the information needed to use Equation 24 to convert the result to dose in Gy/particle:

$$D\left[\frac{Gy}{particle}\right] = \frac{\varepsilon\left[\frac{MeV}{particle}\right] * 1.602E - 13\left[\frac{J}{MeV}\right] * 1000\left[\frac{g}{kg}\right]}{m_{cell}\,[g]}$$

$$\Rightarrow \quad D\left[\frac{Gy}{particle}\right] = \frac{3.64\left[\frac{MeV}{particle}\right]*1.602E-13\left[\frac{J}{MeV}\right]*1000\left[\frac{g}{kg}\right]}{0.0157\,[g]}$$

$$\Rightarrow \quad D\left[\frac{Gy}{particle}\right] = 3.71E-8$$

The error previously converted from 0.02% to 0.07 MeV can be converted to Gy using Equation 24 well:

$$\Rightarrow \quad \sigma\left[\frac{Gy}{particle}\right] = \frac{0.07\left[\frac{MeV}{particle}\right]*1.602E-13\left[\frac{J}{MeV}\right]*1000\left[\frac{g}{kg}\right]}{0.0157\,[g]} = 7.14\text{E-}10$$

The dose in Gy per particle can be converted to Sv using Equation 25:

$$D\,[Sv] = D\left[\frac{Gy}{particle}\right] * \frac{A\,[dps]}{\lambda\,[s^{-1}]}(1 - \exp(-\lambda\tau)) * Y\left[\frac{alphas}{decay}\right] * 20\,[\frac{Sv}{Gy}]$$

$$\Rightarrow \quad D\,[Sv] = 3.71E-8\left[\frac{Gy}{particle}\right] * \frac{1.85E6\,[dps]}{0.0154\,[s^{-1}]}(1 - \exp(-(0.0154*600)) *$$

$$0.969\left[\frac{alphas}{decay}\right] * 20\left[\frac{Sv}{Gy}\right]$$

$$\Rightarrow \quad D\,[Sv] = 86.4$$

The associated error can be converted to Sv with the same equation:

$$\Rightarrow \quad \sigma\,[Sv] = 7.14E-10\left[\frac{Gy}{particle}\right] * \frac{1.85E6\,[dps]}{0.0154\,[s^{-1}]}(1 - \exp(-(0.0154*600)) *$$

$$0.969\left[\frac{alphas}{decay}\right] * 20\left[\frac{Sv}{Gy}\right] = 1.66\,\text{Sv}$$

$$\Rightarrow \quad \boldsymbol{D\,[Sv] = 86.4 \pm 1.66}$$

This matches the dose to Cell 1/Tumor 1 found in Table 10.

5.2.1. Dose per depth

The MCNP results of dose per particle versus tissue depth can be found in Figure 17. As discussed, a second MCNP run was performed with more than 1200 "cells" in 0.1 μm increment depths/volumes in order to make a "dose per depth" plot that could be compared to the analytical model. While MCNP finds dose to specific volumes, the dose per depth plot was created by plotting the dose against the max cell depth.
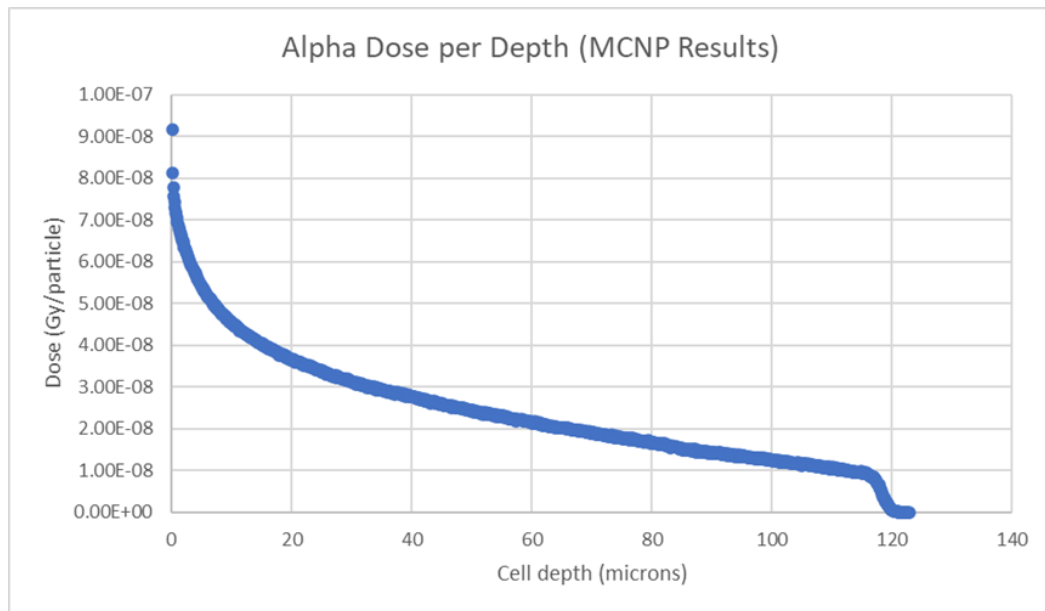

Figure 17: MCNP results for alpha dose as a function of tissue depth.

One of the most notable features of Figure 17 is how the curve drops dramatically as dose per particle gets very close to 0, as opposed to smoothing out gradually to 0 as in the analytical model's results (Fig. 16). One effort to try to limit this behavior close to 0 would be to take steps in variance reduction to try to improve simulation efficiency. MCNP is known for being time-exhaustive with more

complicated radiological scenarios. Variance reduction schemes are used to achieve shorter computational time, therefore increasing efficiency of the simulation.

5.3. Comparison of dose results

Two tables summarizing the dose results from the analytical model and the MCNP model are presented as Tables 11 and 12 below. Table 11 compares the doses to three theoretical tumor volumes (to depths of 50 µm, 100 µm, and 150 µm, or Tumors 1, 2, and 3 respectively), while Table 12 compares the separated dose to each individual stacked cell (0-50 µm or Cell 1, 50-100 µm or Cell 2, and 100-150 µm or Cell 3). Each tumor "begins" at the skin surface and terminates at the maximum depth found in the first column of Table 12. The results for the three tumors are more relevant and applicable to radiation therapy than the results for the individual stacked cells. However, the results in Table 12 provide helpful information that can be used to refine the dosimetry model going forward.

The following tables also provide percent difference of the analytical model as compared to each MCNP calculation. Percent difference is found using Equation 26 below. In this work, the "experimental" values are those achieved by the analytical model, and the "known" values are those from the MCNP simulations.

$$\text{Percent Difference} = \frac{experimental\ value - known\ value}{known\ value} * 100 \quad (26)$$

Table 12: Dose results to three tumor thicknesses, using the analytical dosimetry model and the MCNP model.

"Tumor" max depth	Analytical Cumulative dose (Sv)	MCNP Cumulative dose (Sv)	Difference (Sv)	Difference (%)
Tumor 1: 50 μm	86.8	86.4 (± 1.66)	0.40	(+) 0.46
Tumor 2: 100 μm	59.9	64.0 (± 2.31)	4.10	(-) 6.40
Tumor 3: 150 μm	44.7	45.6 (± 3.17)	0.90	(-) 1.97

Table 11: Dose results to Cells 1-3, using the analytical dosimetry model and the MCNP model.

Cell Dimensions	Analytical Dose to cell (Sv)	MCNP Dose to cell (Sv)	Difference (Sv)	Difference (%)
Cell 1: 0-50 μm	86.8	86.4 (± 1.66)	0.40	(+) 0.46
Cell 2: 50-100 μm	33.1	41.9 (± 1.19)	8.80	(-) 21.0
Cell 3: 100-150 μm	14.2	8.99 (± 0.48)	5.21	(+) 58.0

It can be seen from Table 11 that the analytical dosimetry model described in section 4.3 is generally in good agreement with the MCNP simulation. For each tumor thickness, the results of the analytical model are largely congruent with the MCNP simulations. There is very good agreement in cumulative dose between the analytical and MCNP models for the 50 µm tumor thickness, with a corresponding error of 0.46%, or a difference of 0.40 Sv out of a cumulative dose of roughly 87 Sv for each model. The analytical dose result for the 100 µm tumor thickness has the greatest percentage error of the three tumors. The analytical model under-estimated the MCNP cumulative dose result by 4.10 Sv, or 6.4% of the total MCNP dose of 64.0 Sv.

Of particular importance in Table 11 is the overall low error found between the two models for each of the tumor dose calculations, especially that of the largest tumor, Tumor 3. As mentioned previously, a goal dose of roughly 40-50 Sv to the largest tumor was used to determine dosimetry parameters such as exposure time and source activity. Table 11 shows that this dose was indeed achieved for the MCNP model after the conversion to Sv from the raw results in Gy/particle. The analytical model closely follows the MCNP results for the largest tumor size, which received 44.7 Sv compared to the MCNP result of 45.6 Sv, an under-estimation of 1.97%.

While finding dose to one or more tumor thicknesses is generally the goal of radiation therapy dosimetry, valuable information can be gained by analyzing different aspects of the dose results. Table 12 presents the separate doses to each individual 50 µm stacked cell, Cells 1-3 in Figure 14. While this may have less direct practicality in radiation therapy than the doses to the tumors found in Table 11, Table 12 offers a more

detailed view of how accurately the analytical model estimates dose at specific skin thicknesses.

Because the first stacked cell, Cell 1, has the same dimensions as Tumor 1, the dose results for Tumor 1 and Cell 1 between Tables 11 and 12 are identical for both models. These results are confirmed by hand in the previous sections. As expected, Cells 2 and 3 have diminishing doses as fewer alpha particles are able to irradiate the entire dose-disk due to the shrinking of R_{eff} at higher values of tissue depth h. This is seen for both the analytical and MCNP models.

It can be seen from Table 11 that the greatest difference between the cumulative doses found by the analytical and MCNP models was in the second tumor thickness of 0-100 µm. It is interesting to note that the error associated with the dose to Cell 2 between the two models is more pronounced than that of Tumor 2 in Table 11. The dose to Cell 2 found by the analytical model differed from the MCNP result by 8.80 Sv, equaling an underestimate of 21% of the MCNP dose.

Additionally, the relatively low error of the total cumulative dose to the largest tumor, Tumor 3, in Table 11 greatly contrasts with the more noticeable error found between the analytical and MCNP models for Cell 3 seen in Table 12. This is in part due to the difference in calculated range between the two models. While the MCNP model stops contributing to Cell 3 after 122 µm, the analytical model continues to contribute dose until 165 µm, more than 40 µm after the MCNP model stops.

While the larger errors found in Table 12 do elucidate what parts of the model need further refining, a parameter that is helpful to keep in mind is the actual dose difference that each percentage error represents. This motivates the inclusion of the

column labeled "Difference (Sv)." It is notable that the percent error associated with the dose results to Cell 3 is more than twice that of Cell 2. However, the raw difference in dose between the two models is 8.80 Sv for Cell 2, greater than 5.21 Sv for Cell 3. While the analytical dose estimate to Cell 3 would be considered less accurate than that of Cell 2, the raw dose difference between the models is larger for Cell 2. These factors are very important to consider in radiation dosimetry; without examination and inclusion of all the various elements of the model results, any alterations to the analytical model may make other elements of the model less accurate.

Table 12 shows that the analytical model dose results for Cell 2 and Cell 3, which translate to the "middle" and "deep" portions of the largest (150 µm) tumor thickness, respectively, are more inaccurate than that of Cell 1. This indicates that while the model is in very good agreement with MCNP for Cell 1, it becomes less accurate at predicting dose as the alpha particles reach the end of their tracks. As mentioned, this is largely due to the difference in calculated range between the MCNP and analytical models. Because the alphas in the MCNP model are not able to entirely penetrate the 150 µm tumor depth due to their 122 µm range, the dose to the region of Cell 3 will be much smaller than that of the analytical model, whose alpha particles can theoretically fully penetrate the 150 µm tumor depth. These results are mirrored in the dose per depth result graphs of each model (Figures 16 and 17).

5.4. Comparison of dose per depth graphs

Figure 18 shows a composite graph displaying the dose per depth results of both analytical and MCNP models. Because the raw MCNP results were in units of

MeV/particle, the MCNP dose results were derived using Equations 24 and 25. This will be discussed in more detail.
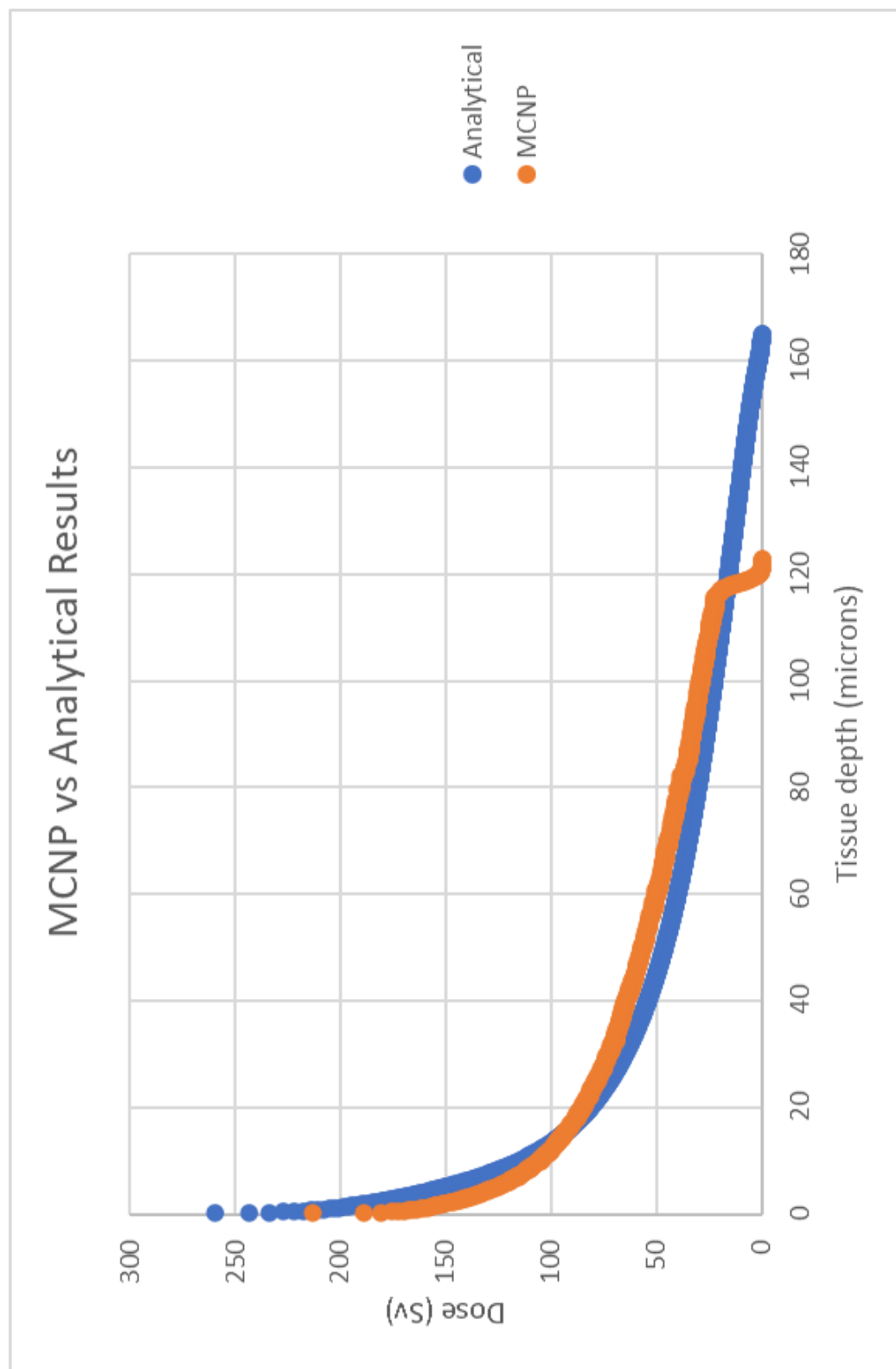
Figure 18: The dose results per micron tissue depth for the analytical model (blue) and MCNP model (unit-adjusted, orange).

As the numeric data showed in section 5.2, the graphical data show that the analytical dosimetry model is in good agreement with the MCNP simulation. The MCNP curve follows the expected shape with dose rapidly dropping in the first ~20 μm of tissue, and then dropping more moderately through the end of the alpha particles' track. The range of ^{212m}Po in tissue was found to be 122 μm in the MCNP model. Around this tissue depth, the MCNP dose drops to zero in a sharp manner. As discussed in section 5.2.1 referring to Figure 17, this dip in the graph is likely in part due to the simulation's reduced ability to estimate dose per particle at rates close to 0, as fewer alpha particles are able to reach those depths. Although the MCNP curve in Figure 18 is a unit-adjusted version of Figure 17, the shape of the curve would not be expected to change between the two figures as the simulation's results are unchanged.

To demonstrate how the values in the graph were achieved, below are step-by-step calculations for the 20 μm tissue depth in the analytical and MCNP models. These calculations follow the same steps as section 5.1. Presented first are the hand-calculations for the analytical model, beginning with the calculation of the average flux factor.

$$\varphi$$

$$= \frac{1}{4\pi(10)}$$

$$* \sum_{n=1}^{10} \ln \left\{ \frac{1 + 0.002^2 - (0.1n)^2 + \sqrt{(1 + 0.002^2 - (0.1n)^2)^2 + 4(0.1n)^2(0.002)^2}}{2(0.002)^2} \right\}$$

$$\Rightarrow \varphi = 0.905$$

This will come into the final dose calculation at the end of the method. The next step is to find the effective radius (Eq. 17) and divide it into ten concentric annuli.

$$R_{\text{eff}} = \sqrt{\Lambda^2 - h^2} = \sqrt{0.0165^2 - 0.002^2} = 0.0164 \text{ cm}$$

The above value is the effective radius as well as the radius of the largest annulus, denoted as $r_{eff,10}$. The value of the effective radius is divided by 10 to get ten equidistant concentric annuli. Each annulus radius is denoted by $r_{eff,i}$.

Annulus radius	[cm]	Annulus radius	[cm]
$r_{\text{eff},1}$	0.00164	$r_{\text{eff},6}$	0.00983
$r_{\text{eff},2}$	0.00328	$r_{\text{eff},7}$	0.0115
$r_{\text{eff},3}$	0.00491	$r_{\text{eff},8}$	0.0131
$r_{\text{eff},4}$	0.00655	$r_{\text{eff},9}$	0.0147
$r_{\text{eff},5}$	0.00819	$r_{\text{eff},10}$	0.0164

From here, the angle θ_i can be calculated for each annulus using Equation 17. The calculation for the angle θ_{10}, corresponding to annulus radius $r_{eff,10}$, can be found below, with the angles corresponding to the other annuli presented in table form.

$$\theta_{10} = \tan^{-1}\left[(0.0164 + \frac{0.0164 - 0.0147}{2}) * \frac{1}{0.002}\right] = 1.44 \text{ radians}$$

θ_i	[radians]	θ_i	[radians]
θ_1	0.389	θ_6	1.35
θ_2	0.888	θ_7	1.39

θ_3	1.12	θ_8	1.41
θ_4	1.23	θ_9	1.43
θ_5	1.31	θ_{10}	1.44

Next, the travel length from the point source to the edge of each annulus, $r_{t,i}$, is found with Equation 18. The calculation of $r_{t,10}$ is shown below, with the other travel lengths presented in a table below.

$$r_{t,10} = \frac{0.002}{\cos(1.44)} = .0157$$

$r_{t,i}$	[cm]	r_t	[cm]
$r_{t,1}$	0.00216	$r_{t,6}$	0.00922
$r_{t,2}$	0.00317	$r_{t,7}$	0.0108
$r_{t,3}$	0.00456	$r_{t,8}$	0.0124
$r_{t,4}$	0.00607	$r_{t,9}$	0.0141
$r_{t,5}$	0.00764	$r_{t,10}$	0.0157

With the path length between the point source and the edge of each annulus known, it is possible to determine residual density range (Eq. 20), and therefore residual energy (Eq. 9) and stopping power of the alpha particle at the edge of each annulus (Eq. 10). Residual density range is calculated at the edge of the largest annulus below, and is presented in table form for the rest of the annuli.

$$(\Lambda\rho)_{res,10} = (0.0165 \text{ [cm]} - 0.0157 \text{ [}cm\text{]}) * 1.00 \text{ [}\tfrac{g}{cm^3}\text{]} = 8.1\text{E-4 g/cm}^2$$

$(\Lambda\rho)_{res,i}$	[g/cm²]	$(\Lambda\rho)_{res,i}$	[g/cm²]
$(\Lambda\rho)_{res,1}$	0.0143	$(\Lambda\rho)_{res,6}$	0.00727
$(\Lambda\rho)_{res,2}$	0.0133	$(\Lambda\rho)_{res,7}$	0.00567
$(\Lambda\rho)_{res,3}$	0.0119	$(\Lambda\rho)_{res,8}$	0.00405
$(\Lambda\rho)_{res,4}$	0.0104	$(\Lambda\rho)_{res,9}$	0.00244
$(\Lambda\rho)_{res,5}$	0.00886	$(\Lambda\rho)_{res,10}$	0.000812

Using the values of residual density range in the above table plugged into Equation 9 to get the residual energy at the edge of each annulus.

E_i	[MeV]	E_i	[MeV]
E_1	10.5	E_6	6.97
E_2	10.0	E_7	5.93
E_3	9.46	E_8	4.75
E_4	8.72	E_9	3.33
E_5	7.89	E_{10}	1.26

The stopping power can then be calculated at the edge of each annulus by plugging the values of residual energy into Equation 10.

$(\frac{S}{\rho})_i$	[MeV·cm²·g⁻¹]	$(\frac{S}{\rho})_i$	[MeV·cm²·g⁻¹]
$(\frac{S}{\rho})_1$	511.1	$(\frac{S}{\rho})_6$	692.7

$$\left(\frac{S}{\rho}\right)_2 \quad 527.9 \qquad \left(\frac{S}{\rho}\right)_7 \quad 776.4$$

$$\left(\frac{S}{\rho}\right)_3 \quad 554.5 \qquad \left(\frac{S}{\rho}\right)_8 \quad 906.8$$

$$\left(\frac{S}{\rho}\right)_4 \quad 589.0 \qquad \left(\frac{S}{\rho}\right)_9 \quad 1154.6$$

$$\left(\frac{S}{\rho}\right)_5 \quad 633.5 \qquad \left(\frac{S}{\rho}\right)_{10} \quad 2031.4$$

As in section 5.1, the stopping power increases dramatically as the particle reaches the edge of the effective radius, which is expected.

The weight of each annulus is found by using Equation 21, which compares the area of the annulus to the area of the entire dose-disk. The weight of the largest annulus ($r_{eff,10}$) is calculated below, with the weights of the rest of the annuli presented in a table below.

$$w_{10} = \frac{\pi(0.0164^2 - 0.0147^2)}{\pi(1)^2} = 5.1E - 5$$

w_i	[unitless]	w_i	[unitless]
w_1	2.69E-6	w_6	2.95E-5
w_2	8.05E-6	w_7	3.49E-5
w_3	1.34E-5	w_8	4.02E-5
w_4	1.88E-5	w_9	4.56E-5
w_5	2.41E-5	w_{10}	5.10E-5

The dose to each annulus that makes up R_{eff} can be found with Equation 22. The dose to the largest annulus is calculated below and the doses to the other annuli presented in table form.

$$\dot{D}_\iota \ [Sv] = \frac{1.6E-10 \left[\frac{J \cdot g}{MeV \cdot kg}\right] * \left(S/\rho\right)_i \left[\frac{MeV \cdot cm^2}{g}\right] * w_i}{4\pi r_t^2 \ [cm^2]}$$

$$* \frac{A \ [dps]}{\lambda \ [s^{-1}]} (1 - \exp(-\lambda t)) * Y \left[\frac{alphas}{decay}\right] * 20 \ [\frac{Sv}{Gy}]$$

$$\dot{D}_{10} = \frac{(1.602E-10) * 2031.4 * 5.1E-5}{4\pi(0.0157)^2} * \frac{1.85E6}{0.0154} (1 - \exp(-0.0154 * 600))$$

$$* 0.969 * 20$$

$$\Rightarrow \dot{D}_{10} = 12.5 \ \text{Sv}$$

D_i	[Sv]	D_i	[Sv]
D_1	8.71	D_6	7.13
D_2	12.6	D_7	6.85
D_3	10.6	D_8	6.99
D_4	8.91	D_9	7.90
D_5	7.78	D_{10}	12.5

Finally, for the total dose to the infinitely thin dose-disk at 20 μm below skin surface, the ten annulus doses are summed and multiplied by the average flux factor (Eq. 23).

$$D = 0.905 * \sum_{i=1}^{10} D_i = \mathbf{81.4\ Sv}$$

We can then compare this result from the analytical model to that of the MCNP

model by converting the energy deposition results at 20 µm to results in Sv. The output

results of the second 1200-cell MCNP run are very long, so the results for only the cell

with the max depth of 20 µm (corresponding to an internal cell number of 210) is shown

below.

```
    7-        c Tallied Skin Cells
    8-        c Main Cells

  208-        210   1      -1      -210   211   -4        IMP:A=1

 6011-        c Surfaces


 6218-        210   py      -0.00199
 6219-        211   py      -0.002

 7521-        MODE A
 7522-        SDEF PAR=A ERG=11.66 POS=0 0.00000001 0 EXT=0 RAD=d2 AXS=0 1 0
 warning.  ext is constant. in most problems it is a variable.
 7523-        SI2      0 1
 7524-        SP2      -21 1
 7525-        c Absorbed Dose
 7526-        *F8:A

                             atom       gram                                   alpha
             cell     mat    density    density    volume      mass       pieces importance

             210          1  9.58192E-02 1.00000E+00 3.14159E-05 3.14159E-05    1  1.0000E+00


1tally       8        nps =     8000000
             tally type 8*   energy deposition                    units   mev
             particle(s): alphas

cell  210
          7.13801E-03 0.0041
```

Much like the way that the cells were described in section 4.4, the same

conventions apply to cell 210. The black boxes represent the surface boundaries and

specifications for the one-micron-wide cell that terminates at 20 µm. The mass of this

cell was found to be 3.14E-5 g and the energy deposition was 7.14E-3 MeV per particle.

These results can be converted to Gy/particle using Equation 24:

$$D\left[\frac{Gy}{particle}\right] = \frac{\varepsilon\left[\frac{MeV}{particle}\right] * 1.602E - 13\left[\frac{J}{MeV}\right] * 1000\left[\frac{g}{kg}\right]}{m_{cell}\,[g]}$$

$$\Rightarrow D\left[\frac{Gy}{particle}\right] = \frac{7.14E-3\left[\frac{MeV}{particle}\right]*1.602E-13\left[\frac{J}{MeV}\right]*1000\left[\frac{g}{kg}\right]}{3.14E-5[g]}$$

$$\Rightarrow D\left[\frac{Gy}{particle}\right] = 3.64E - 8$$

The dose in Gy per particle can be converted to Sv using Equation 25:

$$D\,[Sv] = D\left[\frac{Gy}{particle}\right] * \frac{A\,[dps]}{\lambda\,[s^{-1}]}(1 - \exp(-\lambda\tau)) * Y\left[\frac{alphas}{decay}\right] * 20\,[\frac{Sv}{Gy}]$$

$$\Rightarrow D\,[Sv] = 3.64E - 8\left[\frac{Gy}{particle}\right] * \frac{1.85E6\,[dps]}{0.0154\,[s^{-1}]}(1 - \exp(-(0.0154 * 600))) *$$

$$0.969\left[\frac{alphas}{decay}\right] * 20\left[\frac{Sv}{Gy}\right]$$

$$\Rightarrow D\,[Sv] = 84.8$$

The dose values at 20 µm tissue depth of 81.4 Sv for the analytical model and 84.8 Sv for the MCNP model can be visually confirmed by viewing Figure 18.

The analytical curve of Figure 18 closely follows the same shape as the MCNP curve, with several distinctions. The analytical curve can be seen slightly overshooting

the MCNP curve's initial rapid dose drop until roughly ~18 μm tissue depth. From there, the analytical model continues to follow the same shape as the MCNP curve with slight undershoot until the end of the MCNP calculated range, 122 μm as mentioned previously. While the end of the MCNP curve drops dramatically at the end of its range, the analytical curve continues to moderately decrease until the end of its calculated range, 165 μm.

Figure 18 underscores much of the results that were discussed in section 5.3. Tables 11 and 12 showed that between 0-50 μm (Cell 1/Tumor 1), the analytical model overestimated dose by 0.46%. When viewing Figure 18, one notices the analytical overshoot from roughly zero to 18 μm, followed by an intersection of the curves where the analytical curve begins to slightly undershoot the MCNP curve well past the 50 μm depth boundary. The percent error is hardly quantifiable viewing Figure 18 with the naked eye, which is expected for such a small figure. The small difference between the MCNP and analytical doses to Cell 1/Tumor 1 are certainly reflected in Figure 12. The analytical curve slightly overshoots the MCNP curve for nearly half of Cell 1/Tumor 1, then slightly undershoots through the remainder of the cell. The relatively small difference between the models' dose results is congruent with this pattern.

Table 12 showed that for the tissue depth dimensions of Cell 2, 50-100 μm, the analytical model underestimates overall dose by 21%, or 8.80 Sv. The raw difference (in Sv) between the dose estimate for Cell 2 by the two models is the largest of the three cells. There is a visible gap seen in Figure 12 between the two curves in this tissue depth region, with the analytical curve slightly undershooting through the Cell 2 region. Unlike Cell 1's region on the graph, there are no moments of overshoot to "balance

out" the overall dose estimate, leading to the larger underestimate found in Table 12. This underestimate is therefore consistent with the shape of the analytical curve compared to the MCNP curve seen in Figure 18.

In the last region of the graph, between 100-150 μm or the Cell 3 region, the most evident contrast between the MCNP and analytical curves is caused by the difference in range estimates between both models. As mentioned previously, the MCNP simulation determined the range of ^{212m}Po alpha particles to be about 122 μm, compared to the analytical model's calculated 165 μm. The difference in the calculated range of ^{212m}Po between the two models is ostensibly the main cause of the considerable dose overestimate found for Cell 3 in Table 11.

The period of undershoot for the analytical model from ~100-118 μm indicates that if the MCNP curve were extrapolated closer to the analytical curve's range, the analytical curve would continue this undershoot. Therefore, the error in Cell 3 is not so much an issue of over- or undershoot as was the case with Cells 1 and 2. The error in Cell 3 is certainly almost solely due to the difference in calculated range between the two models. Due to this difference in calculated range, the alpha particles in the analytical model can, theoretically, completely traverse the 150 μm tumor depth and beyond. Therefore, more energy deposition will be detected in this region of interest by the analytical model, leading to a larger dose for the analytical model in this region.

5.4.1. Range comparisons

One of the most significant sources of contrast and error between the MCNP and analytical models is the difference in calculated range for ^{212m}Po alpha particles.

Figure 18 shows the analytical model predicted a range of 165 μm, while the MCNP simulation calculated a range of 122 μm – an overestimation of range by the analytical model of 35%. This warrants further exploration, as the range of the alpha particles in tissue determines the tumor size that can be irradiated by the ^{212m}Po skin patch. While the difference in calculated range does not seem to have a large impact on the dose results between the models to the three theoretical tumors in Table 10, it is important to have an accurate range estimation for any form of radiation therapy before actual patient treatment.

There are no real-world experiments that have empirically determined the range of ^{212m}Po. The National Institute of Standards and Technology (NIST) ASTAR program is a helpful reference tool that determines stopping power and range of alpha particles in various materials (National Institute of Standards and Technology). Alpha particles of 11.66 MeV energy in liquid water were input into the ASTAR program and the results are outlined in Table 13. The liquid water medium in ASTAR has identical density to that of tissue ($\rho = 1$ g/cm^3) which was used in the MCNP and analytical models for range determination. The exact material composition of tissue used in the MCNP simulation can be found in McConn Jr, et al (2011).

Table 13: NIST ASTAR results for stopping power and range for 11.66 MeV alpha particles in liquid water.

ALPHA PARTICLE STOPPING POWER AND RANGE						
WATER, LIQUID						
T = alpha particle (helium ion) kinetic energy, MeV						
STOP(e) = electronic stopping power, MeV cm^2/g						
STOP(n) = nuclear stopping power, MeV cm^2/g						
STOP(t) = total stopping power, MeV cm^2/g						
RANGE(c) = csda range, g/cm^2						
RANGE(p) = projected range, g/cm^2						
DETOUR = detour factor						
T	STOP(e)	STOP(n)	STOP(t)	RANGE(c)	RANGE(p)	DETOUR
1.166E+01	4.758E+02	3.349E-01	4.761E+02	1.460E-02	1.457E-02	9.978E-01

The ASTAR program determines the projected range of these alpha particles to be 145 μm, which lies between the MCNP range determination of 122 μm and the analytical model calculation of 165 μm. It is assumed that the MCNP simulation is more accurate to real-life radiation transport; however, the ASTAR result may indicate that the MCNP range is an underestimate of the actual range.

A factor that may be contributing to the difference in the calculated ranges is the phenomenon of range straggling, which was discussed in section 3.1.4.1. As is seen in Figure 10, the range straggling effect can lead to a projected range that is shorter than the actual observed range. This is a result of large-angle scattering towards the end of the alpha particles' tracks and statistical fluctuations in the number of interactions required to completely slow the alpha particle (Shultis and Faw, 2008). At much higher energies, like that of ^{212m}Po, it is not unusual for the range straggling effect to be more pronounced. It is therefore likely that in addition to difficulty calculating dose near 0,

the MCNP simulation may be presenting a range straggling effect, leading to a shorter range than would be expected from these alpha particles.

Further refinement of range determination is needed for improved external alpha particle radiotherapy. The NCSS software described in section 4.2 may be able to decrease the analytical model's range estimate with an improved fit equation, although more sensitive software may be required to achieve this.

6   Conclusion

In this work, a dosimetry model was presented with the intention of calculating dose to theoretical early-stage NMSC skin tumors from high-energy alpha particles emitted from ^{212m}Po. The analytical model and the MCNP simulation were generally in good agreement for alpha particle dose determinations to three tumor depths, with the analytical dose result to the largest 150 μm tumor underestimating the MCNP dose result by 0.90 Sv, or 1.97%.

This work showed that the concept of using high-energy alpha particle emitters in a radioactive skin patch to treat NMSC tumors is valid. The 11.66 MeV alpha particle emissions of ^{212m}Po were able to irradiate the entirety of the epidermis as measured at most body sites (Whitton, 1977; Sevcova et al, 1978), and this was shown in both models. Therapeutic doses of 40-50 Sv were able to be calculated to the largest tumor thickness using a radioactivity and exposure time that were reasonable for radiotherapy treatments. Another potential application of the alpha-emitting skin patch is use post-operatively to irradiate any cancer cells that may be left over after surgery.

Further improvements can be made to the model for more accurate dose results. A major contributing factor to the difference in results between the two models is the difference in range determination. Improved fit equations could be used to more closely approximate the MCNP simulation for better results. Additionally, future improvements to MCNP may enhance the program's ability to accurately determine range.

While there is still much research related to alpha emitters, their general availability and radiochemistry that still need to be made before they are regularly used in external radiotherapy, this work has shown that alpha emitters do have the ability to penetrate NMSC tumors and deliver therapeutic doses to them.

Bibliography

Allen, B, et al. (2005). Intralesional targeted alpha therapy for metastatic melanoma. *Cancer Biology & Therapy*, *4*(12), 1318-1324.

American Academy of Dermatology. (2020). SKIN CANCER TYPES: BASAL CELL CARCINOMA SIGNS AND SYMPTOMS. Retrieved from https://www.aad.org/public/diseases/skin-cancer/types/common/bcc/symptoms

American Academy of Dermatology. (2020). SKIN CANCER TYPES: SQUAMOUS CELL CARCINOMA SYMPTOMS. Retrieved from https://www.aad.org/public/diseases/skin-cancer/types/common/scc/symptoms

American Joint Committee on Cancer. (2010). *AJCC Cancer Staging Manual* (Seventh ed.). New York, NY: Springer Science + Business Media.

Apalla, Z, et al. (2017, April). Epidemiological trends in skin cancer. In *National Center for Biotechnology Information (NCBI)*. Retrieved from https://www.ncbi.nlm.nih.gov/pmc/articles/PMC5424654/

Ascierto, P. A., & Schadendorf, D. (2019, March). Immunotherapy in non-melanoma skin cancer: updates and new perspectives. In *National Center for Biotechnology Information (NCBI)*. Retrieved from https://www.ncbi.nlm.nih.gov/pmc/articles/PMC6434981/#

Betts, J. G., et al (2013). *Anatomy and Physiology*. N.p.: OpenStax.

Chung, Y. L. (2000, July). Treatment of Bowen's disease with a specially designed radioactive skin patch. *European Journal of Nuclear Medicine*, *27*(7).

Dourmishev, L. A., Rusinova, D., & Botev, I. (2013). Clinical variants, stages, and management of basal cell carcinoma. In *National Center for Biotechnology Information (NCBI)*. Retrieved from https://www.ncbi.nlm.nih.gov/pmc/articles/PMC3573444/#

Eatough, J. P. (1997). Alpha-particle dosimetry for the basal layer of the skin and the radon progeny 218-Po and 214-Po. *Physics in Medicine & Biology*, *42*, 1899-1911.

Eatough, J. P., & Henshaw, D. L. (1992). Radon and thoron associated dose to the basal layer of the skin. *Physics in Medicine & Biology*, *37*.

Fahradyan, A, et al. (2017, December). Updates on the Management of Non-Melanoma Skin Cancer (NMSC). In *National Center for Biotechnology Information (NCBI)*. Retrieved from https://www.ncbi.nlm.nih.gov/pmc/articles/PMC5746716/#

Hamby, D. M., & Mangini, C. D. (2018). VARSKIN 6: A Computer Code for Skin Contamination Dosimetry.

Harvey, J. (1971). Alpha Radiation, an External Radiation Hazard? *Health Physics*, *21*(6).

Heller, J. (2019, September). Skin layers. In *MedLinePlus*. Retrieved from https://medlineplus.gov/ency/imagepages/8912.htm

International Atomic Energy Agency (IAEA) – Nuclear Data Section. Live Chart of Nuclides. Vienna International Centre, Vienna, Austria.

International Commission on Radiological Protection (ICRP), 2007. The 2007 Recommendations of the International Commission on Radiological Protection. ICRP Publication 103. Ann. ICRP 37 (2-4).

Knoll, G. F. (2000). *Radiation Detection and Measurement* (3rd ed.). N.p.: John Wiley and Sons.

Jeong, J. (2003), et al. Preparation of 188Re-labeled paper for treating skin cancer. *Applied Radiation and Isotopes*, *58*, 551-555.

Kim, Y., & Brechbiel, M. W. (2012). An overview of targeted alpha therapy. *Tumor Biology*, *33*, 573-590.

Lassmann, M., & Eberlein, U. (2017). Targeted alpha-particle therapy: imaging, dosimetry, and radiation protection. *ICRP 2017 Proceedings*, 187-195.

Lee, J, et al. (1997, May). Radionuclide Therapy of Skin Cancers and Bowen's Disease Using a Specially Designed Skin Patch. *The Journal of Nuclear Medicine*, *38*(5).

Lock-Andersen, J, et al. (1997). Epidermal thickness, skin pigmentation and constitutive photosensitivity. *Photodermatology Photoimmunology & Photomedicine*, *13*, 153-158.

McConn Jr, R, et al. (2011). 321 Tissue, Soft (ICRU Four Component). In *Compendium of Material Composition Data for Radiation Transport Modeling*. Richland, WA: Pacific Northwest National Laboratory.

Misdaq, M. A., & Harrass, H. (2017). Determination of Alpha Radiation Dose to Skin Due to Artificial and Natural Radionuclides from the Deposition of Different Material Samples. *International Journal of Engineering Research and Technology*, *10*(1), 1-18.

Mukherjee, A, et al. (2003, October). Bioevaluation of radioactive bandages in a murine model of melanoma. *International Journal of Radiation Biology*, *79*(10), 839-845.

Munaweera, I, et al. (2014). Radiotherapeutic Bandage Based on Electrospun Polyacrylonitrile Containing Holmium-166 Iron Garnet Nanoparticles for the Treatment of Skin Cancer. *ACS Applied Materials & Interfaces*, *6*, 22250-22256.

National Cancer Institute. (n.d.). Layers of the Skin. In *SEER Training Modules*. Retrieved from https://training.seer.cancer.gov/melanoma/anatomy/layers.html

National Institute of Standards and Technology. (n.d.). ASTAR. In *National Institute of Standards and Technology Physical Measurement Laboratory*. Retrieved from https://physics.nist.gov/PhysRefData/Star/Text/ASTAR.html

NCSS 2020 Statistical Software (2020). NCSS, LLC. Kaysville, Utah, USA, ncss.com/software/ncss.

Pashazadeh, A, et al. (2019, November). Radiation therapy techniques in the treatment of skin cancer: an overview of the current status and outlook. *Journal of Dermatological Treatment*, *30*(8), 831-839.

Pashazadeh, A, et al. (2018). Conceptual design of a personalized radiation therapy patch for skin cancer. *Current Directions in Biomedical Engineering*, *4*(1), 607-610.

Salgueiro, M. J. (2008). Design and bioevaluation of a 32P-patch for brachytherapy of skin diseases. *Applied Radiation and Isotopes*, *66*, 303-309.

Samarasinghe, V., & Madan, V. (2012). Nonmelanoma Skin Cancer. In *National Center for Biotechnology Information (NCBI)*. Retrieved from https://www.ncbi.nlm.nih.gov/pmc/articles/PMC3339125/

Sandby-Moller, J, et al. (2003). Epidermal Thickness at Different Body Sites: Relationship to Age, Gender, Pigmentation, Blood Content, Skin Type and Smoking Habits. *Acta Dermato-Venereologica*, *83*, 410-413

Sevcova, M. (1978). Alpha Irradiation of the Skin and Possibility of Late Effects. *Health physics*, *35*(6), 803-806.

Sevcova, M, et al. (1978). On the thickness of the epidermis. *Ceskoslovenska dermatologie*, *53*(4), 223-228.

Sgouros, G, et al. (2010). MIRD Pamplet No.22 (Abridged): Radiobiology and Dosimetry of alpha-Particle Emitters for Targeted Radionuclide Therapy. *Journal of Nuclear Medicine*, *51*, 311-328.

Shultis, J. K., & Faw, R. E. (2008). *Fundamentals of Nuclear Science and Engineering* (2nd ed.). Boca Raton, FL: Taylor & Francis Group.

Turner, J. (2007). *Atoms, Radiation, and Radiation Protection* (3rd ed.). N.p.: Wiley-VCH.

Whitton, J. T. (1973). New Values for Epidermal Thickness and Their Importance. *Health physics*, *24*(1), 1-8.

Woolsey, Adam. (2018). Investigation of the Thermal Neutron Diffusion Length in Graphite. 10.13140/RG.2.2.12415.87206.

Yousef, H. (2020). Anatomy, Skin (Integument), Epidermis. In *National Center for Biotechnology Information (NCBI)*. Retrieved from https://www.ncbi.nlm.nih.gov/books/NBK470464/

Appendix A: Abridged ICRU 90 (2014) Stopping Power and Range Data

I = 78.0 eV; ρ = 0.998 g/cm^3				I = 85.7 eV; ρ = 0.0012 g/cm^3		
alpha particles in liquid water				alpha particles in air		
	Mass Stopping	Density			Mass Stopping	Density
Energy	Power, S_t/ρ	Range		Energy	Power, S_t/ρ	Range
(MeV)	(MeV cm^2 g^{-1})	(g cm^{-2})		(MeV)	(MeV cm^2 g^{-1})	(g cm^{-2})
0.001	3.271E+02	3.273E-06		0.001	2.215E+02	5.377E-06
0.0015	3.306E+02	4.789E-06		0.0015	2.342E+02	7.562E-06
0.002	3.343E+02	6.294E-06		0.002	2.445E+02	9.651E-06
0.003	3.436E+02	9.247E-06		0.003	2.622E+02	1.360E-05
0.004	3.546E+02	1.211E-05		0.004	2.784E+02	1.730E-05
0.005	3.666E+02	1.489E-05		0.005	2.937E+02	2.079E-05
0.006	3.793E+02	1.757E-05		0.006	3.084E+02	2.411E-05
0.008	4.049E+02	2.267E-05		0.008	3.363E+02	3.032E-05
0.01	4.304E+02	2.746E-05		0.01	3.624E+02	3.605E-05
0.015	4.916E+02	3.831E-05		0.015	4.225E+02	4.879E-05
0.02	5.483E+02	4.793E-05		0.02	4.765E+02	5.992E-05
0.03	6.506E+02	6.462E-05		0.03	5.720E+02	7.900E-05
0.04	7.411E+02	7.900E-05		0.04	6.557E+02	9.530E-05
0.05	8.229E+02	9.179E-05		0.05	7.309E+02	1.097E-04
0.06	8.979E+02	1.034E-04		0.06	7.998E+02	1.228E-04
0.08	1.032E+03	1.241E-04		0.08	9.230E+02	1.460E-04
0.1	1.150E+03	1.425E-04		0.1	1.032E+03	1.665E-04
0.15	1.397E+03	1.817E-04		0.15	1.257E+03	2.101E-04
0.2	1.593E+03	2.151E-04		0.2	1.437E+03	2.472E-04
0.3	1.881E+03	2.725E-04		0.3	1.699E+03	3.108E-04
0.4	2.068E+03	3.230E-04		0.4	1.866E+03	3.667E-04
0.5	2.183E+03	3.699E-04		0.5	1.965E+03	4.188E-04
0.6	2.244E+03	4.150E-04		0.6	2.011E+03	4.690E-04
0.8	2.260E+03	5.034E-04		0.8	2.005E+03	5.682E-04
1	2.193E+03	5.931E-04		1	1.924E+03	6.698E-04
1.5	1.879E+03	8.385E-04		1.5	1.627E+03	9.518E-04
2	1.600E+03	1.128E-03		2	1.383E+03	1.286E-03
3	1.240E+03	1.844E-03		3	1.072E+03	2.115E-03
4	1.022E+03	2.737E-03		4	8.864E+02	3.147E-03
5	8.754E+02	3.798E-03		5	7.611E+02	4.368E-03
6	7.693E+02	5.020E-03		6	6.700E+02	5.772E-03
8	6.243E+02	7.924E-03		8	5.456E+02	9.101E-03
10	5.294E+02	1.142E-02		10	4.637E+02	1.309E-02
15	3.896E+02	2.258E-02		15	3.425E+02	2.581E-02

Appendix B: MCNP6 Run Specifications and Abridged Output Results

```
1mcnp     version 6     ld=02/20/18              11/01/20 16:14:09
 **************************************************************              probid =  11/01/20 16:14:09
 n=MCNP_alpha_transport_October_2.txt


   comment.  Physics models enabled.
        1-        Alpha Dose
        2-        c cell cards for sample problem
        3-        1 0    -1 11 -3 IMP:A=1           $ void above skin
        4-        2 1 -1 2 -14 -3 IMP:A=1 $ skin behind tally skin
        5-        3 1 -1 -11 14 -3 7 IMP:A=1        $ skin to the side of talled skin
        6-        4 0 1:-2:3  IMP:A=0
        7-        c Tallied Skin Cells
        8-        c Main Cells
        9-        11   1       -1      -11   12    -4       IMP:A=1
       10-        12   1       -1      -12   13    -4       IMP:A=1
       11-        13   1       -1      -13   14    -4       IMP:A=1
       12-        21   1       -1      -11   12    4    -5     IMP:A=1
       13-        22   1       -1      -12   13    4    -5     IMP:A=1
       14-        23   1       -1      -13   14    4    -5     IMP:A=1
       15-        31   1       -1      -11   12    5    -6     IMP:A=1
       16-        32   1       -1      -12   13    5    -6     IMP:A=1
       17-        33   1       -1      -13   14    5    -6     IMP:A=1
       18-        41   1       -1      -11   12    6    -7     IMP:A=1
       19-        42   1       -1      -12   13    6    -7     IMP:A=1
       20-        43   1       -1      -13   14    6    -7     IMP:A=1
       21-
       22-        c Surfaces
       23-        1       py  1
       24-        2       py  -1
       25-        3       cy  10
       26-        4       cy  1
       27-        5       cy  1.005
       28-        6       cy  1.01
       29-        7       cy  1.015
       30-        11    py      0
       31-        12    py      -0.005
       32-        13    py      -0.01
       33-        14    py      -0.015
       34-
       35-        MODE A
       36-        SDEF PAR=A ERG=11.66 POS=0 0.00000001 0 EXT=0 RAD=d2 AXS=0 1 0
 warning.  ext is constant. in most problems it is a variable.
       37-        SI2      0 1
       38-        SP2      -21 1
       39-        c Absorbed Dose
       40-        *F8:A   11 12 13 21 22 23 31 32 33 41 42 43
       41-        M1   1001.24c -0.101172

                           atom      gram                                      alpha
            cell     mat   density   density    volume       mass      pieces importance

          1      1       0  0.00000E+00 0.00000E+00 3.14159E+02 0.00000E+00     1  1.0000E+00
          2      2       1  9.58192E-02 1.00000E+00 3.09447E+02 3.09447E+02     1  1.0000E+00
          3      3       1  9.58192E-02 1.00000E+00 4.66384E+00 4.66384E+00     1  1.0000E+00
          4      4       0  0.00000E+00 0.00000E+00 0.00000E+00 0.00000E+00     0  0.0000E+00
          5     11       1  9.58192E-02 1.00000E+00 1.57080E-02 1.57080E-02     1  1.0000E+00
          6     12       1  9.58192E-02 1.00000E+00 1.57080E-02 1.57080E-02     1  1.0000E+00
          7     13       1  9.58192E-02 1.00000E+00 1.57080E-02 1.57080E-02     1  1.0000E+00
          8     21       1  9.58192E-02 1.00000E+00 1.57472E-04 1.57472E-04     1  1.0000E+00
          9     22       1  9.58192E-02 1.00000E+00 1.57472E-04 1.57472E-04     1  1.0000E+00
         10     23       1  9.58192E-02 1.00000E+00 1.57472E-04 1.57472E-04     1  1.0000E+00
         11     31       1  9.58192E-02 1.00000E+00 1.58258E-04 1.58258E-04     1  1.0000E+00
         12     32       1  9.58192E-02 1.00000E+00 1.58258E-04 1.58258E-04     1  1.0000E+00
         13     33       1  9.58192E-02 1.00000E+00 1.58258E-04 1.58258E-04     1  1.0000E+00
         14     41       1  9.58192E-02 1.00000E+00 1.59043E-04 1.59043E-04     1  1.0000E+00
         15     42       1  9.58192E-02 1.00000E+00 1.59043E-04 1.59043E-04     1  1.0000E+00
         16     43       1  9.58192E-02 1.00000E+00 1.59043E-04 1.59043E-04     1  1.0000E+00

 total                                           6.28319E+02 3.14159E+02


1tally       8     nps =    30000000
        tally type 8*   energy deposition                        units   mev
        particle(s): alphas

 cell  11
             3.63633E+00 0.0002

 cell  12
             1.76482E+00 0.0003

 cell  13
             3.78344E-01 0.0006
```

```
cell  21
              1.08980E-02 0.0042

cell  22
              6.35565E-03 0.0056

cell  23
              9.75197E-04 0.0128

cell  31
              3.93748E-03 0.0072

cell  32
              1.87018E-03 0.0100

cell  33
              2.33291E-05 0.0774

cell  41
              3.13502E-04 0.0222

cell  42
              1.19562E-05 0.1079

cell  43
              0.00000E+00 0.0000
```

```
=========================================================================================================================

         results of 10 statistical checks for the estimated answer for the tally fluctuation chart (tfc) bin of tally       8

tfc bin     --mean--    ---------relative error---------    ----variance of the variance----    --figure of merit--   -pdf-
behavior    behavior    value   decrease   decrease rate    value   decrease   decrease rate    value     behavior    slope

desired     random      <0.10    yes       1/sqrt(nps)      <0.10    yes         1/nps          constant   random     >3.00
observed    random      0.00     yes          yes           0.00     yes          yes          constant   random     10.00
passed?      yes        yes      yes          yes            yes     yes          yes            yes        yes        yes

=========================================================================================================================

this tally meets the statistical criteria used to form confidence intervals: check the tally fluctuation chart to verify.
the results in other bins associated with this tally may not meet these statistical criteria.

----- estimated confidence intervals:  -----

estimated asymmetric confidence interval(1,2,3 sigma): 3.6355E+00 to 3.6372E+00; 3.6347E+00 to 3.6380E+00; 3.6338E+00 to 3.6388E+00
estimated  symmetric confidence interval(1,2,3 sigma): 3.6355E+00 to 3.6372E+00; 3.6347E+00 to 3.6380E+00; 3.6338E+00 to 3.6388E+00

1analysis of the results in the tally fluctuation chart bin (tfc) for tally 8 with nps = 30000000            print table 160


normed average tally per history  = 3.63633E+00          unnormed average tally per history  = 3.63633E+00
estimated tally relative error    = 0.0002               estimated variance of the variance  = 0.0000
relative error from zero tallies  = 0.0002               relative error from nonzero scores  = 0.0001

number of nonzero history tallies =    14999023          efficiency for the nonzero tallies  = 0.5000
history number of largest  tally =           4           largest  unnormalized history tally = 1.16600E+01
(largest  tally)/(average tally)  = 3.20653E+00          (largest   tally)/(avg nonzero tally)= 1.60316E+00

(confidence interval shift)/mean  = 0.0000               shifted confidence interval center  = 3.63633E+00


                       tally      8
        nps     mean      error   vov  slope    fom
     2048000  3.6398E+00 0.0009 0.0000 10.0  261752
     4096000  3.6392E+00 0.0006 0.0000 10.0  254839
     6144000  3.6382E+00 0.0005 0.0000 10.0  254630
     8192000  3.6370E+00 0.0004 0.0000 10.0  257563
    10240000  3.6374E+00 0.0004 0.0000 10.0  260527
    12288000  3.6368E+00 0.0004 0.0000 10.0  260319
    14336000  3.6366E+00 0.0003 0.0000 10.0  258134
    16384000  3.6371E+00 0.0003 0.0000 10.0  258725
    18432000  3.6369E+00 0.0003 0.0000 10.0  257009
    20480000  3.6364E+00 0.0003 0.0000 10.0  257049
    22528000  3.6365E+00 0.0003 0.0000 10.0  256560
    24576000  3.6362E+00 0.0003 0.0000 10.0  255772
    26624000  3.6365E+00 0.0002 0.0000 10.0  255017
    28672000  3.6364E+00 0.0002 0.0000 10.0  255531
    30000000  3.6363E+00 0.0002 0.0000 10.0  255149


run terminated when    30000000  particle histories were done.
```